Available online at www.sciencedirect.com
ScienceDirect
Ocean Modelling 15 (2006) 274–298
Ocean Modelling
www.elsevier.com/locate/ocemod

Spatial and temporal structure of Tropical Pacific interannual variability in 20th century coupled simulations

Antonietta Capotondi [a,*], Andrew Wittenberg [b], Simona Masina [c]

[a] NOAA/Earth System Laboratory, CIRES/Climate Diagnostics Center, R/CDC1, 325 Broadway, Boulder, CO 80305, United States
[b] Geophysical Fluid Dynamics Laboratory, Princeton, NJ, United States
[c] Istituto Nazionale di Geofisica e Vulcanologia, Bologna, Italy

Received 27 May 2005; received in revised form 6 February 2006; accepted 7 February 2006
Available online 9 March 2006

Abstract

Tropical Pacific interannual variability is examined in nine state-of-the-art coupled climate models, and compared with observations and ocean analyses data sets, the primary focus being on the spatial structure and spectral characteristics of El Niño-Southern Oscillation (ENSO). The spatial patterns of interannual sea surface temperature (SST) anomalies from the coupled models are characterized by maximum variations displaced from the coast of South America, and generally extending too far west with respect to observations. Thermocline variability is characterized by dominant modes that are qualitatively similar in all the models, and consistent with the "recharge oscillator" paradigm for ENSO. The meridional scale of the thermocline depth anomalies is generally narrower than observed, a result that can be related to the pattern of zonal wind stress perturbations in the central-western equatorial Pacific. The wind stress response to eastern equatorial Pacific SST anomalies in the models is narrower and displaced further west than observed. The meridional scale of the wind stress can affect the amount of warm water involved in the recharge/discharge of the equatorial thermocline, while the longitudinal location of the wind stress anomalies can influence the advection of the mean zonal temperature gradient by the anomalous zonal currents, a process that may favor the growth and longer duration of ENSO events when the wind stress perturbations are displaced eastwards. Thus, both discrepancies of the wind stress anomaly patterns in the coupled models with respect to observations (narrow meridional extent, and westward displacement along the equator) may be responsible for the ENSO timescale being shorter in the models than in observations. The examination of the leading advective processes in the SST tendency equation indicates that vertical advection of temperature anomalies tends to favor ENSO growth in all the CGCMs, but at a smaller rate than in observations. In some models it can also promote a phase transition. Longer periods tend to be associated with thermocline and advective feedbacks that are in phase with the SST anomalies, while advective tendencies that lead the SST anomalies by a quarter cycle favor ENSO transitions, thus leading to a shorter period.

Keywords: El Niño phenomena; Climatic changes; Permanent thermocline; Winds; Surface temperature

Regional terms: Tropical Pacific Ocean

* Corresponding author. Tel.: +1 303 497 6105; fax: +1 303 497 6449.
E-mail address: Antonietta.Capotondi@noaa.gov (A. Capotondi).

1463-5003/$ - see front matter © 2006 Elsevier Ltd. All rights reserved.
doi:10.1016/j.ocemod.2006.02.004

1. Introduction

Tropical Pacific variability plays a fundamental role in the global climate. Not only can the El Niño-Southern Oscillation (ENSO) phenomenon have large economic and societal impacts within the Tropics, but tropical teleconnections forced by diabatic heating of the atmosphere as a response to sea surface temperature (SST) anomalies in the Tropics may affect the seasonal climate in midlatitudes (Alexander et al., 2002). On decadal timescales, SST anomalies in the tropical Pacific and Indian Oceans are associated with widespread anomalies in SST, sea level pressure (SLP), and precipitation (Deser et al., 2004), and may create the conditions for synchronized droughts over extensive areas of the Northern Hemisphere midlatitudes (Hoerling and Kumar, 2003). Thus, a realistic simulation of Tropical Pacific variability is crucial for climate models.

Several state-of-the-art coupled general circulation models (CGCMs) have recently completed simulations of the 20th century, with the purpose of testing the model performance, and assessing their suitability for predicting the climate of the 21st century. Results from these model simulations will be used by the Intergovernmental Panel on Climate Change (IPCC) in their Assessment Report Four (AR4). The primary purpose of this paper is to test the performance of the climate models used for the AR4 in their simulation of Tropical Pacific interannual variability during the 20th century.

Aspects of ENSO that coupled models have had difficulty in simulating realistically include amplitude and spatial structure, dominant timescale, and the relationship between ENSO events and the annual cycle (AchutaRao et al., 2000; Latif et al., 2001; AchutaRao and Sperber, 2002; Davey et al., 2000, 2002; Hannachi et al., 2003). Coupled climate models seem to be characterized by interannual variations that are too regular and have a period shorter than observed (AchutaRao et al., 2000), but the factors that determine the oscillation period are still unclear. The periodicity of ENSO has been related to the spatial pattern and amplitude of the anomalous zonal wind stress (Kirtman, 1997; An and Wang, 2000; Wittenberg, 2002; Deser et al., 2005). Using an intermediate coupled model, which included a 1–1/2 layer ocean component coupled to a statistical atmosphere, Kirtman (1997) has shown that the meridional scale of the wind stress can influence the duration of ENSO events. In his model, the negative feedback for the reversal of the ENSO cycle is provided by equatorial Rossby waves reflecting at the western boundary as equatorial Kelvin waves. Extra-equatorial Rossby waves excited by the wind stress curl in the 5°–15°S latitude band tend to counteract that negative feedback. A meridionally broader anomalous wind stress pattern can excite extra-equatorial Rossby waves over a wider latitude band, leading to a larger range of wave transit times toward the equator and to a longer duration of the reversal phase of the ENSO cycle.

An and Wang (2000) have explained the decrease in ENSO frequency after the mid-seventies in terms of changes in the structure of the anomalous zonal wind stress, the major changes being the broadening of the meridional scale of the wind stress anomalies after the mid-seventies, and the eastward migration of the wind stress anomaly center. Using an intermediate coupled model, they have shown that the longitudinal location of the anomalous zonal wind stress can influence the ENSO timescale through zonal advection of mean zonal temperature gradients by the anomalous zonal currents associated with the anomalous equatorial winds. Depending upon the location of the zonal currents, this anomalous zonal advection process, defined as the "zonal advective feedback" can act as a positive feedback promoting ENSO growth, or can instead favor an ENSO phase transition. The results of the intermediate coupled model showed that an eastward (westward) displacement of the zonal wind stress anomalies (and associated currents) results in a zonal advective feedback that is in phase (in quadrature) with the SST anomalies, thus acting as an ENSO destabilizer (transitioner). Deser et al. (2005) have related the quasi-biennual ENSO timescale in the Community Climate System Model Version 3 (CCSM3) to the very narrow meridional scale of the anomalous wind stress and weaker wind coupling relative to observations. ENSO characteristics, including its period, can also be expected to depend upon the mean state of the system, as defined by the mean depth and slope of the equatorial thermocline, and upon the strength of the mean trade winds (Fedorov and Philander, 2000; Wittenberg, 2002).

The availability of a large number of coupled integrations provides a unique opportunity to examine the dependence of the ENSO timescale upon aspects of the model climatologies and wind stress coupling, thus offering some insight about possible causes of model deficiencies. The intercomparison of several CGCMs can also reveal whether dynamical processes emphasized by previous studies carried out with simpler coupled systems can control Tropical Pacific interannual variability in complex coupled models as well. The specific

questions that we ask in this study are: (1) What is the spatial and temporal structure of ENSO in the various climate models? (2) Can we relate the ENSO timescale to specific dynamical processes? and (3) How realistically are these processes represented in the models, and what is the relative importance of these processes in the different models? The ENSO timescale is believed to be determined by the slower (relative to the atmosphere) oceanic processes, including wave propagation and anomalous equatorward transports, which may be well described by the temporal evolution of the equatorial thermocline depth. While some of the previous intercomparison studies have focussed on SST variability and related atmospheric fields, we will also examine the leading modes of thermocline variability to achieve a better understanding of the dominant dynamical processes underlying interannual variability. Tropical Pacific variability in some of the models analyzed here has been examined in other studies (Wittenberg et al., 2006; Deser et al., 2005). The intercomparison of the different models performed in this paper will help assess whether the aspects of the variability and dominant mechanisms identified in individual models are robust across different CGCMs.

The paper is organized as follows: in Section 2 we list and briefly describe the models analyzed in this study, and the observational data sets used for their validation. Section 3 describes the spatial patterns of SST, thermocline depth, and wind stress anomalies, as well as the spectral characteristics of ENSO, while in Section 4 the relative importance of the dynamical processes that control Tropical Pacific SSTs is examined in the different models. Conclusions are drawn in Section 5.

2. CGCMs and observational datasets

Nine CGCMs are used for this study. A list of the models, and information about their spatial resolution and period covered by the simulations are given in Table 1. Since one of our major foci is the ENSO timescale, the CGCMs are sorted in Table 1 by decreasing period (Table 2). The model outputs have been collected at the Program for Climate Model Diagnosis and Intercomparison (PCMDI). There is a wide range of resolutions and numerical grid types among the models. Some of the models have an irregular grid for the ocean component. For example, the ocean component of CCSM3 is based on the Parallel Ocean Program (POP), and uses a bipolar grid with the northern pole displaced over Greenland. The IPSL-CM4 model uses a tripolar ocean grid, with two poles in the northern hemisphere, one over Canada, and the other over Siberia. Most ocean components have a finer meridional grid spacing in the Tropics to resolve the jet-like structure of the equatorial circulation, as described in Table 1. The model outputs were interpolated on a regular longitude–latitude grid before been archived at PCMDI. All the models used for this study, with the exception of the MRI-CGCM2.3.2, have no flux adjustments. The MRI-CGCM2.3.2 applies a seasonally varying correction to the tropical wind stress (http://www.mri-jma.go.jp/Dep/cl/cl4/IPCC-AR4/model.html).

The initial conditions for the 20th century integrations were taken from long control simulations with a fixed pre-industrial greenhouse concentration. The simulations were then run forward using full greenhouse and volcanic forcing over the 20th century. In some cases a small ensemble (3–7 members) of 20th century

Table 1
List of the models used in this study, including information about atmospheric and tropical oceanic resolutions (longitude × latitude × # of vertical layers) and period covered by the 20th century simulation

Model #	Model	Institution	Ocn. resolution	Atm. resolution	Period
1	INGV	INGV (Italy)	0.5° × 0.5°L31		1958–2000
2	GFDL/ARCs	GFDL (USA)	1° × 1°L40		1980–2000
3	UKMO-HadCM3	Hadley Center (UK)	1.25° × 1.25°L20	3.75° × 2.5°L19	1860–1999
4	PCM	NCAR (USA)	0.66° × 0.5°L32	T42L18	1890–1999
5	GISS-EH	NASA/GISS (USA)	2° × 2°L16	5° × 4°L20	1880–1999
6	CNRM-CM3	Météo-France/CNRM (France)	2° × 0.5L31	T63L45	1860–1999
7	CSIRO-Mk3.0	CSIRO (Australia)	1.875° × 0.84°L31	T63L18	1871–2000
8	MRI-CGCM2.3.2	MRI (Japan)	2.5° × 0.5°L23	T42L30	1851–2000
9	GFDL-CM2.0	GFDL (USA)	1° × 0.33°L50	2.5° × 2.°L24	1861–2000
10	IPSL-CM4	IPSL (France)	2° × 0.5°L31	2.5° × 3.75°L19	1860–2000
11	CCSM3	NCAR (USA)	1.125° × 0.27°L40	T85L26	1870–1999

Table 2
Interannual timescale (T), meridional width of the zonally-averaged τ^x regressed upon the Niño3.4 index (L_y), amplitude of the interannual zonal wind stress (τ) normalized by the standard deviation of the Niño3.4 index, "center of mass" of τ^x regressed upon the Niño3.4 index (C), and period predicted using a multiple regression algorithm that relates T to C and L_y (Eq. (2)), for the INGV ocean analysis and the CGCMs

Model	T (year)	L_y (°Latitude)	τ (mPa °C^{-1})	C (°E)	T_p (year)
INGV	4.1	23.6	5.5	192	4.28
UKMO-HadCM3	3.7	14.2	6.0	189	3.20
PCM	3.4	13.8	3.6	186	3.06
GISS-EH	3.3	15.6	3.5	189	3.35
CNRM-CM4	3.2	12.6	5.5	190	3.07
CSIRO-Mk3.0	3.2	11.4	4.5	187	2.84
MRI-CGCM2.3.2	2.6	15.6	5.7	171	2.74
GFDL-CM2.0	2.5	14.9	4.4	163	2.40
IPSL-CM4	2.3	12.0	4.2	188	2.94
CCSM3	2.2	9.9	4.5	185	2.62

All the quantities are defined in the text. The ocean analyses and the CGCMs are sorted by period.

integrations is available, the different members starting at different times of the control simulation. In this study we will focus on one ensemble member per model, since there is no consistency in the ensemble size among the models, and for some models only one simulation is available.

To validate the models we use SST data from the National Oceanic and Atmospheric Administration Extended Reconstruction of Historical Sea Surface Temperature (NOAA.ERSST) archive, available at the NOAA-CIRES Climate Diagnostics Center (http://www.cdc.noaa.gov/). Surface wind stresses are from the National Center for Environmental Prediction–National Center for Atmospheric Research (NCEP–NCAR) Reanalysis product (Kistler et al., 2001).

To assess the degree of realism of the evolution of thermocline depth we use data from two different ocean analyses: the first one is the Geophysical Fluid Dynamics Laboratory/Applied Research Centers (GFDL/ARCs) product, in which observed SST and vertical temperature profiles are assimilated into the Modular Ocean Model version 4 (MOM4), run at a horizontal resolution of 1°, and telescoping to 1/3° in the equatorial region, using the three-dimensional variational scheme of Derber and Rosati (1989). The model was forced with time varying winds over the period 1980–2000, consisting of a wind stress climatology derived from the NASA/DAO/SSMI analysis for the period 1987–1996 (Atlas et al., 1996), and anomalous wind stress from the NCEP/NCAR Reanalyses (Kistler et al., 2001). The second ocean analysis product is from the Istituto Nazionale di Geofisica e Vulcanologia (INGV, Bologna Italy, Masina et al., 2004). Surface and subsurface temperature data are assimilated into an eddy-permitting version of MOM (horizontal grid spacing is 0.5° in longitude, and increases in latitude from 1/3° in the 10°S–10°N latitude band to 0.5° close to the northern and southern boundaries of the domain) using a univariate variational optimal interpolation scheme which is conceptually similar to the one described by Derber and Rosati (1989). The model is forced with wind fields from the NCEP–NCAR Reanalyses over the period 1958–2000 (Kalnay et al., 1996). We consider two different data assimilation products to achieve a more robust description of the subsurface temperature field, which may reflect differences in model resolution, details of the assimilation procedure, surface forcing, and duration of the period covered by the assimilation.

3. Spatial structure and spectral characteristics

3.1. SST

The standard deviation of interannual SST from the CGCMs is compared in Fig. 1 with that of observed SSTs. The standard deviations for both observed and modeled SSTs was computed after removing the climatological annual cycle at each spatial point. The pattern of SST variations from observations has maximum values of 1.25–1.5°C, which are found along the coast of South America, and extend westward to ~130°W, with decreasing amplitude. The spatial structure of SST variations differs considerably among different models

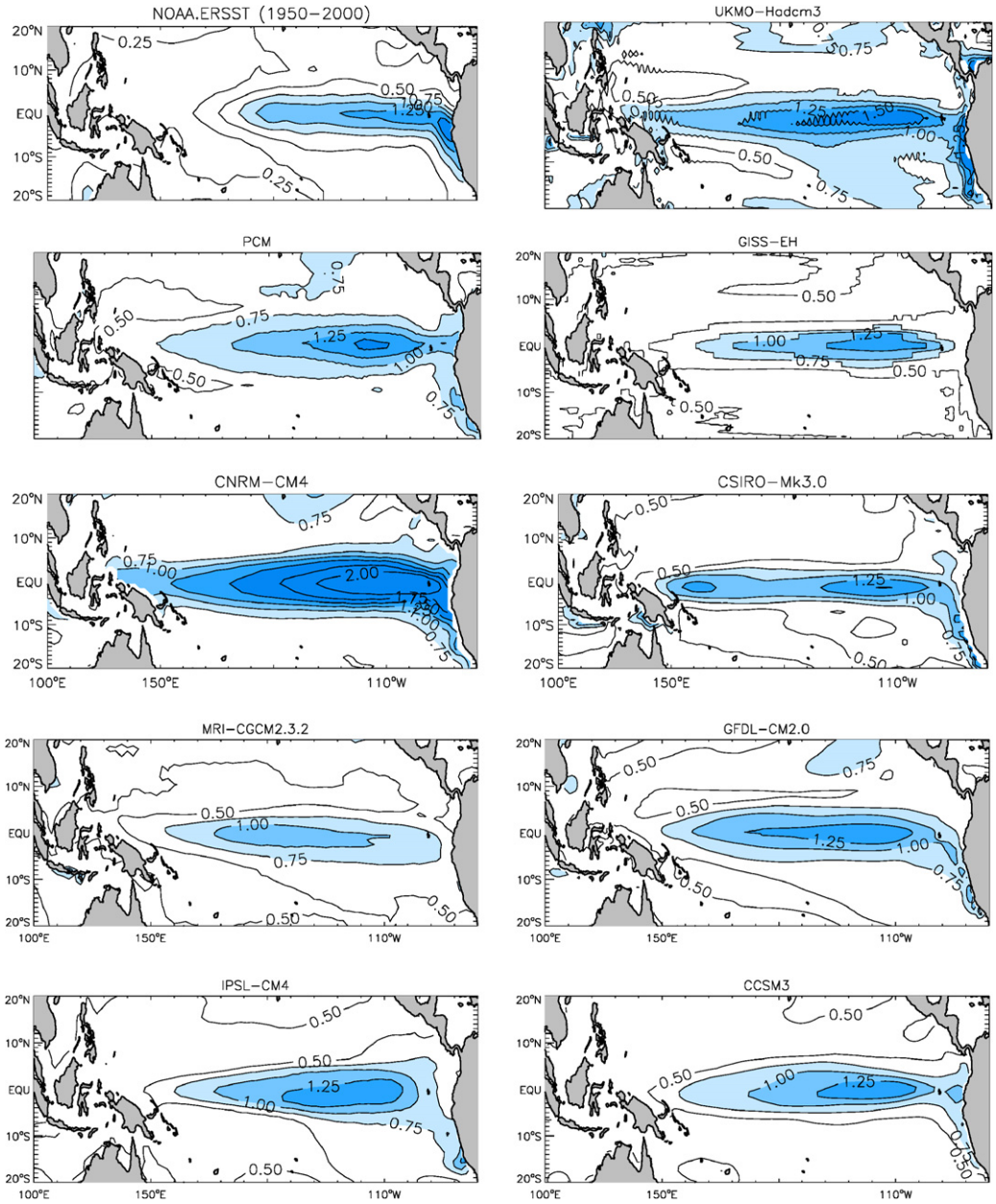

Fig. 1. Standard deviation of interannual SST from observations (top-left) and different CGCMs. In all cases the interannual SSTs have been computed by subtracting the monthly climatology from the monthly averages of the model outputs. Contour interval is 0.25 °C. Values larger than 0.75 °C are shaded. The CGCMs are sorted by decreasing period (see Table 2).

in its meridional and zonal scales, amplitude, and zonal position of maximum variability. With respect to observations, in most CGCMs maximum SST standard deviations are found away from the eastern boundary. The UKMO-HadCM3 exhibits large variability along the coast of South America, with a second broad maximum centered at ~115°W. In most models, interannual SST anomalies extend too far west with respect to observations. Extreme cases are the CNRM-CM3, UKMO-HadCM3, and CSIRO-Mk3.0, where large standard deviations are found all the way to the western boundary. In particular, the CNRM-CM3 has unrealistically large SST anomalies all across the basin, while the CSIRO-Mk3.0 exhibits a maximum centered at ~120°W, and a secondary maximum around 160°E. Most models have temperature variations that are in the

observed range, with maxima of ~1.2–1.5 °C. Two exceptions are the MRI-CGCM2.3.2, whose interannual variations appear to be weaker than the observed variations, and the CNRM-CM3 whose values of standard deviations are much larger than observed.

3.2. Spectral characteristics

To illustrate the time evolution of SST in the eastern equatorial Pacific, the Niño3.4 indices for three CGCMs (CCSM3, GFDL-CM2.0, and GISS-EH) are shown in Fig. 2, where they are compared with the index derived from the NOAA.ERSST dataset (Fig. 2a). Visual inspection of the time series is sufficient to capture the different 'flavors' of ENSO in the CGCMs compared to the observations. CCSM3 (Fig. 2b) is characterized by a quasi-regular 2-year cycle, with an average amplitude which is close to that of the observed time series. The standard deviation of the Niño3.4 index for CCSM3 is 0.93 °C, while for the observational record it ranges from 0.83 °C over the period 1880–2000 to 0.91 °C over the period 1950–2000, the latter being the period characterized by more observations. The GFDL-CM2.0 (Fig. 2c) exhibits SST variations that occur more irregularly than in CCSM3, and seem to have a longer periodicity, but their amplitude appears to be larger than observed (the standard deviation of the Niño3.4 index for GFDL-CM2.0 is 1.14 °C). Finally, GISS-EH (Fig. 2d) is characterized by El Niño and La Niña events occurring irregularly and with varying durations, but the standard deviation of the time series (0.66 °C) is weaker than observed.

To better quantify the spectral characteristics of ENSO, we compute the power spectra of the Niño3.4 time series for all the CGCMs. The Niño3.4 index from observations (Fig. 3a) shows a broad spectrum with a

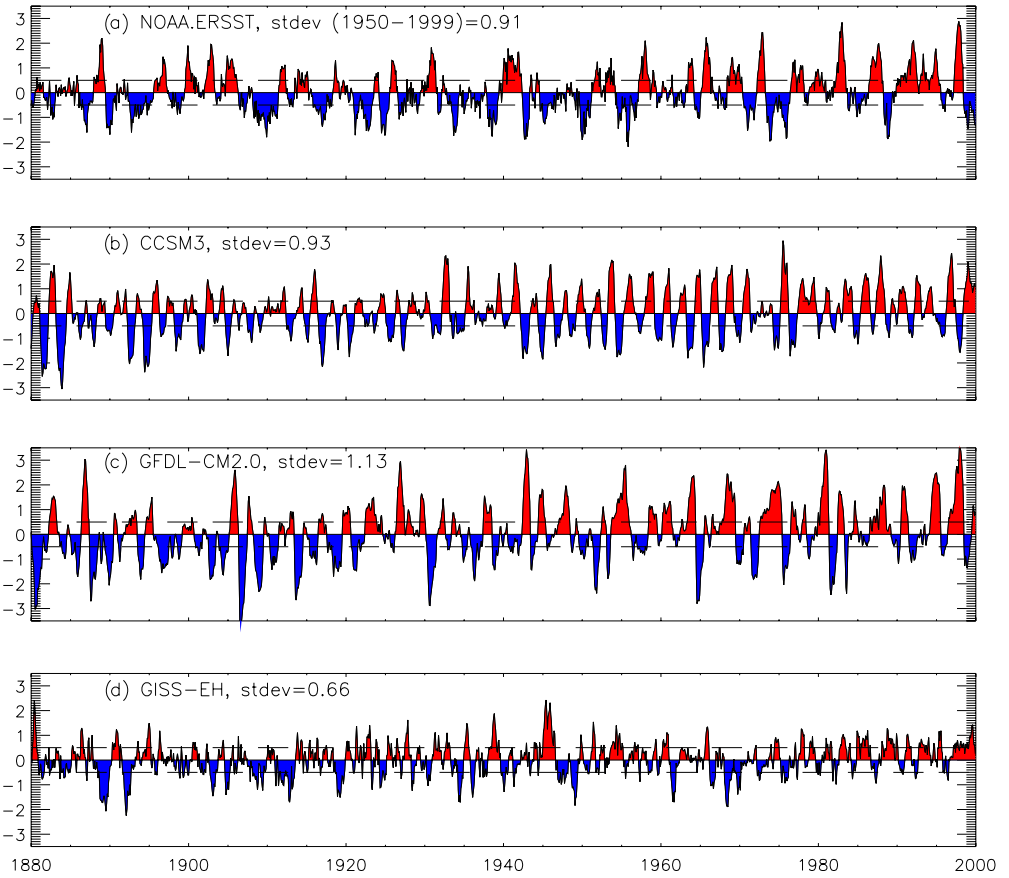

Fig. 2. Evolution of the Niño3.4 index (area-average SST over the region 5°S–5°N, 170°–120°W) for observations (a), CCSM3 (b), GFDL-CM2.0 (c), and GISS-EH (d). The climatological seasonal cycle has been removed, and a 5-month boxcar (equal weighted) smoother has been applied, according to Trenberth (1997). The horizontal dashed lines indicate ±0.5 °C.

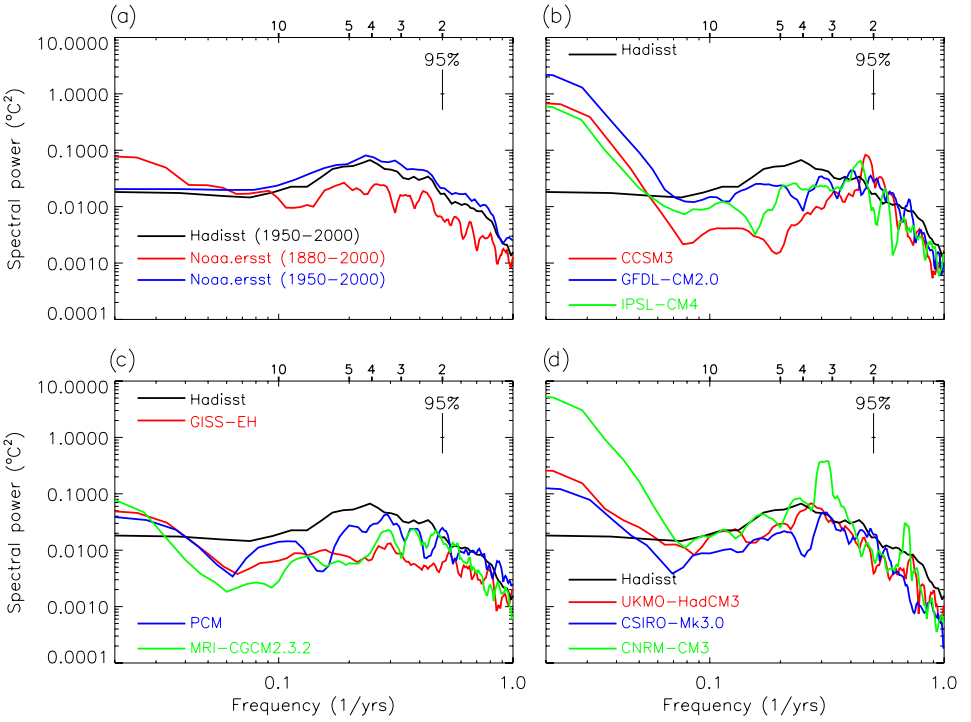

Fig. 3. (a) Power spectra of the Niño3.4 index derived from different observational datasets: HadISST, over the period 1950–2000 (black line), NOAA.ERSST over the period 1880–2000 (red line), and NOAA.ERSST over the period 1950–2000 (blue line). (b) Power spectra of the Niño3.4 index from CCSM3 (red), GFDL-CM2.0 (blue), and IPSL-CM4 (green). The spectrum from the HadISST dataset is shown for comparison. (c) Same as in (b), but for GISS-EH (red), PCM (blue), and MRI-CGCM2.3.2 (green). (d) Same as in (b), but for UKMO-HadCM3 (red), CSIRO-Mk3.0 (blue), and CNRM-CM3 (green). The numbers on the top axis indicate the period in years.

maximum at ~4–4.5 years. The HadISST and NOAA.ERSST yield very similar power spectra over the period (1950–2000). The spectrum from NOAA.ERSST over the period 1880–2000 is also shown to offer some indication of the influence of the duration of the period considered. Over the longer period, the spectrum shows decreased power, a result which may also depend upon the increasing sparseness of data before 1950. The spectra of the Niño3.4 indices from the nine CGCMs are shown in Fig. 3b–d. The dominant timescale for all the models is shorter than observed, ranging from ~2 years for CCSM3 to ~3.7 years for UKMO-HadCM3. There are differences in the width and amplitudes of the spectra. For example, IPSL-CM4 has maximum power around 2.3 years, similar to CCSM3, but relatively larger power levels between 2.5 and 5 years (as well as 10 years) than CCSM3. Notice the very large spectral peak of CNRM-CM3, consistent with the very energetic ENSO-like variability in this model (Fig. 1). The ENSO "period" for each model has been estimated from the Niño3.4 spectra, as the timescale shorter than 10 yrs corresponding to the maximum power. The results are summarized in Table 2.

3.3. Thermocline depth

Some studies have highlighted how the cyclic nature of ENSO arises from the imbalance between the equatorial zonal wind stress anomalies and the zonally averaged anomalous heat content along the equator (Schneider et al., 1995; Kirtman, 1997). Variations in heat content are associated with changes in the depth of the thermocline, which can be viewed as the surface bounding the volume of upper ocean warm water. Variations in zonally averaged thermocline depth originate, in turn, from the anomalous mass convergence/divergence to/from the equator, leading to a mass recharge/discharge process (Jin, 1997a,b). Using subsurface observations over the period 1980–1999, Meinen and McPhaden (2000) have shown that the magnitude of ENSO SST variations is directly related to the zonally averaged anomalies of warm water volume.

Following Meinen and McPhaden (2000) we compute empirical orthogonal functions (EOFs) of thermocline depth for the ocean analysis products and the CGCMs to identify the dominant modes of thermocline variability. We use the depth of the 15 °C isotherm as proxy for thermocline depth. This isotherm is located in the middle-lower thermocline (Fig. 4), so that depth variations are less affected by surface diabatic processes, thus providing a good indication of thermocline variability for all the models, including those with a shallower thermocline. Comparison of the mean temperature section along the equator from the INGV ocean analysis (Fig. 4a) with the climatology of the Tropical Atmosphere Ocean (TAO) buoy array (McPhaden et al., 1998, Fig. 4b) shows that the INGV ocean analysis provides a realistic structure of the mean thermocline at depths shallower than 300 m, where the TAO data are denser. There are differences in the depth of the 15 °C isotherm, as well as thermocline structure, among the CGCMs (Fig. 4). For example, GISS-EH (Fig. 4e), MRI-CGCM2.3.2 (Fig. 4h), and, most notably, PCM (Fig. 4d) have a thermocline which is shallower than the INGV ocean analysis (and TAO data), while UKMO-HadCM3 (Fig. 4c) has a deeper and more diffuse thermocline than the INGV analysis. The depth of the 15 °C isotherm in CCSM3 is in very good agreement with the data assimilation product. These differences in mean thermocline structure should be kept in mind when interpreting the maps of thermocline variability, and comparing the model responses to the wind stress forcing.

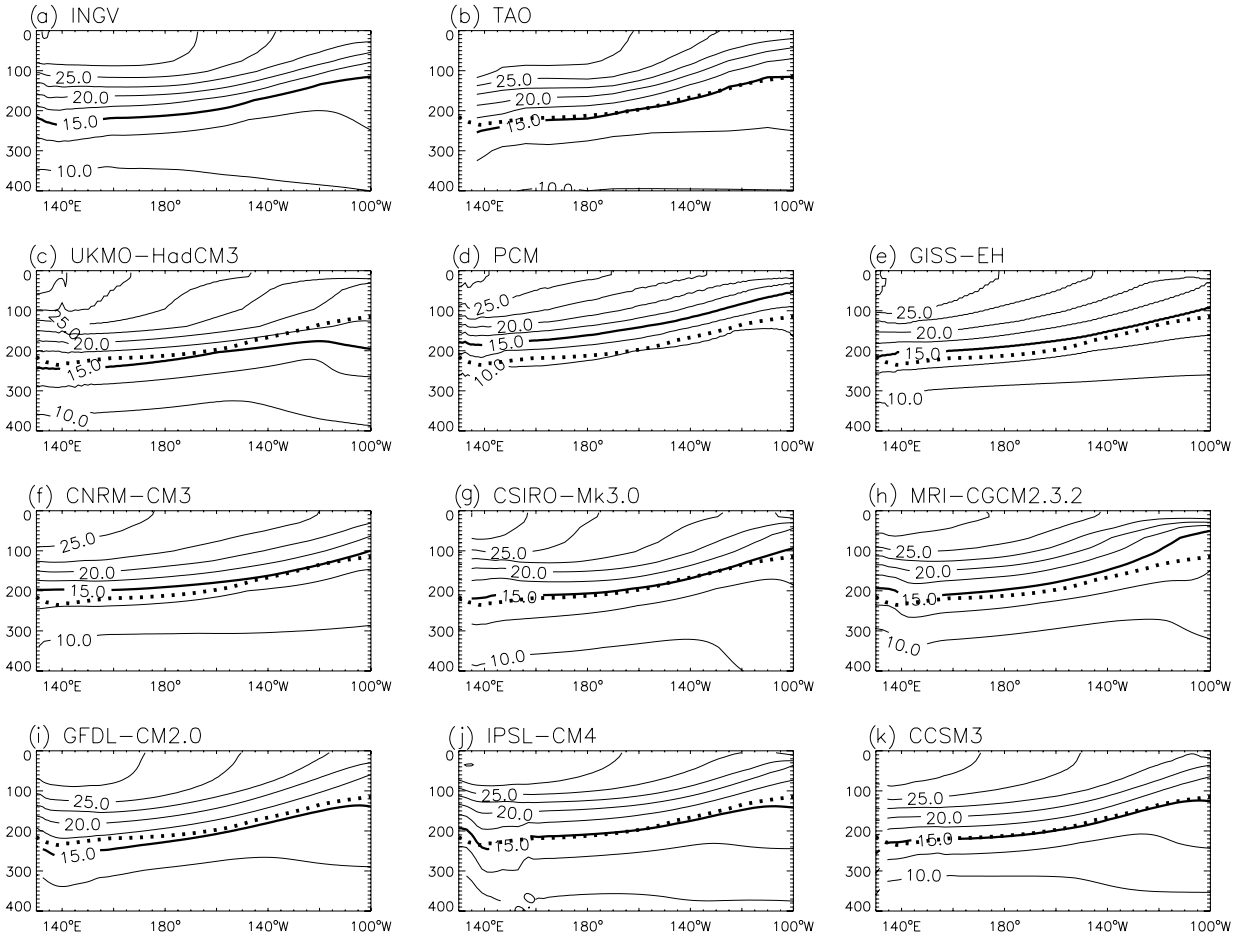

Fig. 4. Mean temperature sections along the equator for the INGV ocean analysis (a), the TAO observations (b), and the nine CGCMs (c–k). Contour interval is 2.5 °C. The thick solid line in each panel highlights the 15 °C isotherm. The 15 °C isotherm from the INGV analysis is shown in panels (b–k) as a dotted line for comparison. The section from the TAO buoy data has been obtained using linear interpolation.

The thermocline depth data have been band-pass filtered prior to the EOF calculation, using a Fourier filter with half-power at 15 months and 7.5 years. The two leading EOFs for the INGV and GFDL/ARCs analyses are shown in Fig. 5a, a′ and b, b′, respectively. In both cases the first EOF has a zonal dipole structure, with anomalies of opposite signs at the eastern and western sides of the basin, thus expressing variations in the zonal slope of the thermocline. The second EOF, on the other hand, has anomalies of the same sign along the equator, describing variations of the zonally averaged thermocline depth. The EOFs from both data assimilation products are very similar to those computed by Meinen and McPhaden (2000, their Fig. 3), although the GFDL/ARCs tends to underestimate the amplitude of the thermocline depth anomalies compared to the observed. In both analyses, EOF-2 has a node along 5°–7°N, the latitude of the North Equatorial Counter-Current (NECC), as in the EOF-2 from observations, while in the Southern Hemisphere the anomalies have a much broader structure, reaching south of 20°S between the dateline and 120°W.

The leading modes of thermocline variability are consistent with the 'recharge oscillator' paradigm for ENSO (Jin, 1997a,b). According to the recharge oscillator hypothesis, a positive SST anomaly in the eastern equatorial Pacific is associated with westerly zonal wind stress anomalies in the central-western Pacific. The weakening of the trade winds along the equator further reduces the zonal thermocline tilt (''Bjerknes positive feedback'', Bjerknes, 1969). A reduced zonal gradient of thermocline depth is associated, by geostrophy, with anomalous poleward flow in the thermocline, resulting in a discharge of warm water from the equatorial thermocline, and leading to a shallower zonally averaged thermocline depth. The shoaling of the thermocline reduces the positive SST anomaly in the east, and the associated wind stress anomaly. Due to the upwelling of colder than average water, a negative SST anomaly eventually develops in the east, thus changing the phase of the oscillation. In this scenario, the SST anomaly in the eastern equatorial Pacific should be in quasi-balance with the anomalous thermocline tilt, and approximately in quadrature with the phases of maximum variations of zonally averaged thermocline depth.

A useful index to describe SST variations in the eastern equatorial Pacific associated with ENSO is the area-averaged SST in the region 5°S–5°N, 170°W–120°W, known as the Niño3.4 index. The time evolution of the two EOFs (Principal Components, PCs) for the INGV analysis are shown in Fig. 6a, together with the Niño3.4 index. The evolution of the Niño3.4 index follows very closely that of PC1 of thermocline depth. The correlation between the two time series is 0.96, with the Niño3.4 index leading PC1 by 1 month. On inter-annual timescales the two time series can be considered practically in phase. Thus, positive (negative) SST anomalies in the eastern equatorial Pacific are associated with a reduced (enhanced) zonal thermocline slope. Fig. 6a′ shows the lag-correlation between PC1 and PC2. The largest correlations, in absolute value, are found at lags of −9 months (PC1 lead PC2), and 9 months (PC2 leads PC1). In the first case, the correlation is negative, indicating that PC1 leads the negative phase of PC2 by 9 months: a reduced zonal thermocline tilt is associated with a decreased equatorward mass transport, resulting in depletion of the warm water volume in the equatorial thermocline, and shallower thermocline depth. The positive correlation at +9 months, on the other hand, indicates that a deeper thermocline (increased warm water volume) leads (by ∼9 months) the positive El Niño phase, in agreement with the findings of Meinen and McPhaden (2000), and consistent with the hypothesis that changes in warm water volume, zonally averaged across the Pacific, are good predictors for ENSO (Wyrtki, 1985; Cane et al., 1986).

What is the structure of the dominant modes of thermocline variability for the CGCMs? Fig. 5c, c′–k, k′ shows the two leading EOFs for all the nine models considered in this study. The structure of the modes is qualitatively similar for all the models, and in agreement with that of the ocean analysis products (and observations, e.g. Meinen and McPhaden, 2000): the first mode expresses variations in the zonal thermocline tilt, while the second mode describes changes in zonally averaged thermocline depth. However, there are significant differences in the detailed structure of the EOFs. In general, the meridional scale of the equatorial anomalies in the CGCMs, especially in EOF-2, is narrower than in the ocean analyses and observations. The differences are primarily found in the Southern Hemisphere, where the CGCMs seem to be unable to fully reproduce the southward extension of the thermocline depth anomaly. In some models (GFDL-CM2.0, PCM, CSIRO), the positive thermocline anomaly in EOF-2 extends south of 20°S east of 180°–160°W, with a pattern that is reminiscent of the EOF structure from the assimilated data sets (Fig. 5a′ and b′). Other models (CCSM3, GISS-EH, IPSL), on the other hand, exhibit a nodal line along ∼10°S. Other differences concern the spatial distribution of variance along the equatorial band in EOF-2. While in the observations the largest

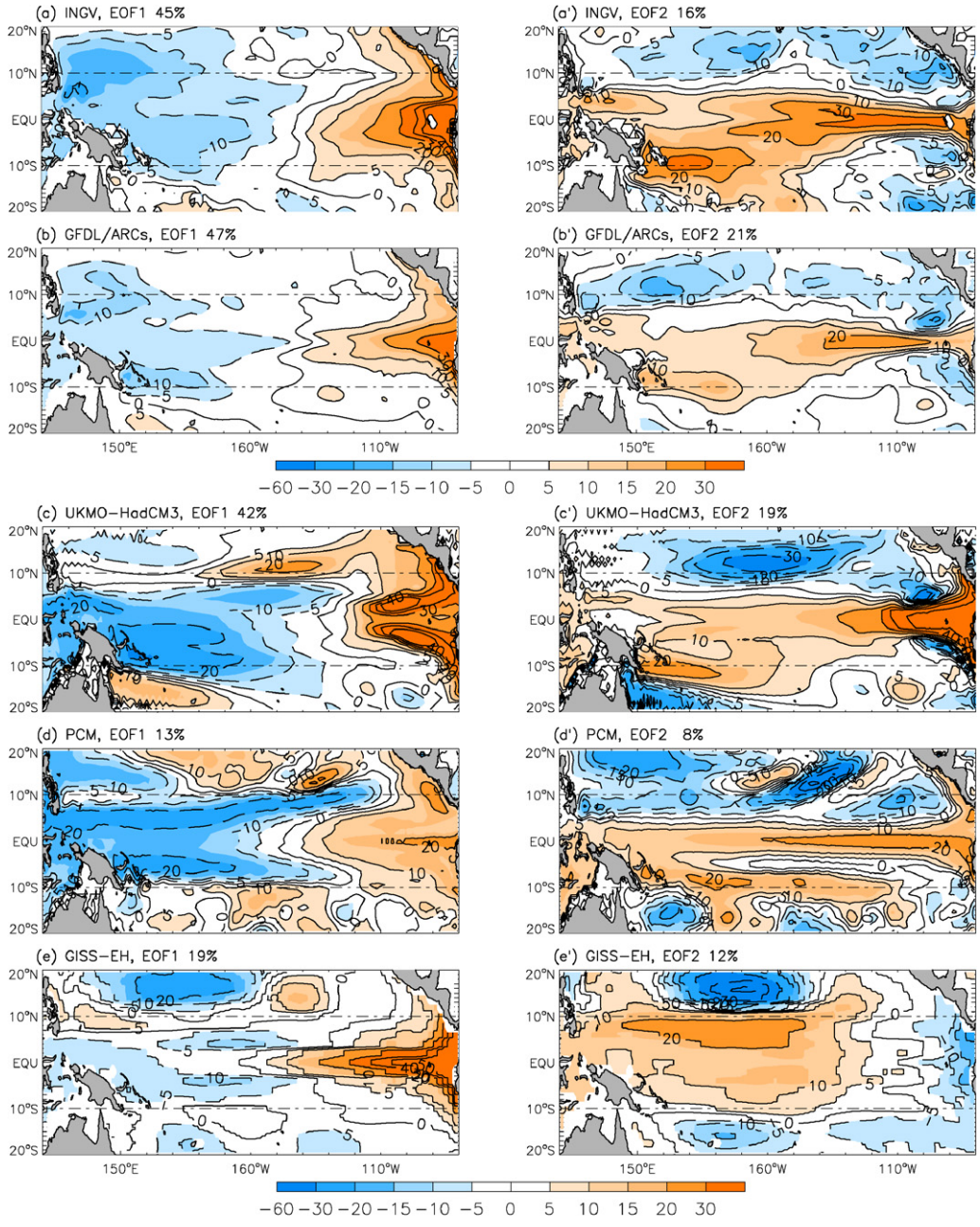

Fig. 5. Leading eofs of thermocline depth (diagnosed as the depth of the 15 °C isotherm) for the INGV ocean analysis, covering the period 1958–2000 (top), and for the GFDL/ARCs analysis over the period 1980–2000 (bottom). Negative values (blue shading) indicate shallower than average thermocline, while positive values (orange shading) indicate deeper than average thermocline. Contour interval is 10 m, but the −5 m and +5 m contours are also indicated. Dot-dash lines in all panels indicate the 10°S and 10°N latitudes for reference. (c) Same as in (a) but for the UKMO-HadCM3 model. (c′) Same as in (a′), but for the UKMO-HadCM3 model. (d) Same as in (a) but for the PCM. (d′) Same as in (a′) but for the PCM. (e) Same as in (a), but for GISS-EH. (e′) Same as in (a′) but for GISS-EH. (f) Same as in (a) but for the CNRM-CM3 model. (f′) Same as in (a′), but for the CNRM-CM3 model. (g) Same as in (a) but for the CSIRO-Mk3.0. (g′) Same as in (a′) but for the CSIRO-Mk3.0. (h) Same as in (a), but for MRI-CGCM2.3.2. (h′) Same as in (a′) but for MRI-CGCM2.3.2. (i) Same as in (a) but for the GFDL-CM2.0 model. (i′) Same as in (a′), but for the GFDL-CM2.0 model. (j) Same as in (a) but for IPSL-CM4. (j′) Same as in (a′) but for IPSL-CM4. (k) Same as in (a), but for CCSM3. (k′) Same as in (a′), but for CCSM3.

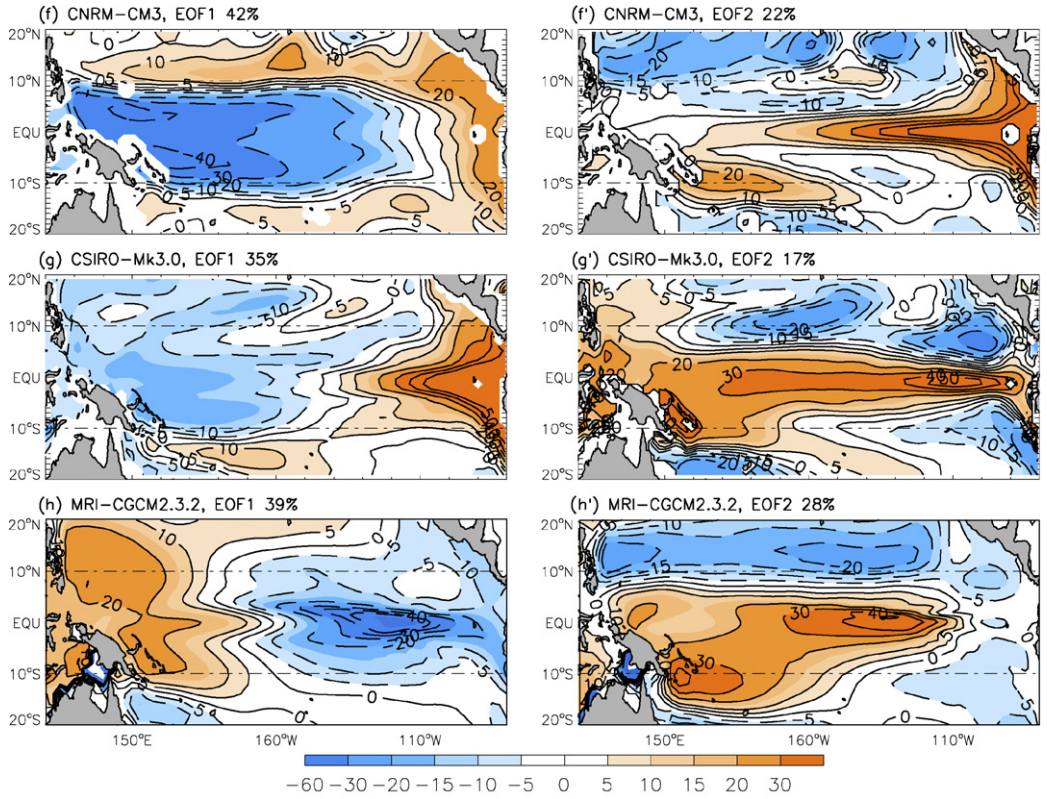

Fig. 5 (*continued*)

values of EOF2 are found in the central-eastern Pacific, some models (GISS-EH, MRI-CGCM2.3.2) have the largest anomalies displaced toward the western Pacific, with very little, or negative loading close to the eastern boundary. In particular, the center of action of EOF-2 in GISS-EH is located north of the equator, between ~150°E and 150°W. In most of the models the combined variance explained by the two leading EOFs accounts for more than 50% of the interannual variance (60–70% in the ocean analyses). Two exceptions are GISS-EH and PCM, where the variance explained by the first two modes is 31% and 21%, respectively.

The time evolution of the leading modes of thermocline variability is consistent with the "recharge oscillator" paradigm for all the models. As examples, the PCs from CCSM3 and UKMO-HadCM3 are shown in Fig. 6b and c, respectively. CCSM3 has a quasi-biennual ENSO, while the UKMO-HadCM3 is characterized by a dominant timescale which is close to 4 years (Fig. 3). The PCs from the two CGCMs are displayed for the years 1958–2000, the same period covered by the INGV analysis. In both cases the Niño3.4 index is highly correlated with PC1, as for the INGV analysis. The lag-correlation between PC1 and PC2 (Fig. 6b′ and c′) exhibits an approximate quadrature relationship for both models, as described for the INGV ocean analysis. The difference in the lags of maximum correlations between CCSM3 and UKMO-HadCM3 reflects the difference of the ENSO periods in the two models. Although the leading modes of thermocline variability are consistent with the "recharge oscillator" paradigm for both ocean analyses and CGCMs, a complete heat budget of the upper ocean in the eastern equatorial Pacific would be necessary to demonstrate that the thermocline anomalies have a controlling influence upon the SST anomalies.

3.4. Surface wind stress

The recharge oscillator theory relates the recharge/discharge process to the anomalous tilt of the equatorial thermocline, which is assumed to be in balance with the anomalous zonal wind stress in the central-western equatorial Pacific (τ^x). The meridional scale of τ^x can be expected to determine the meridional width of the

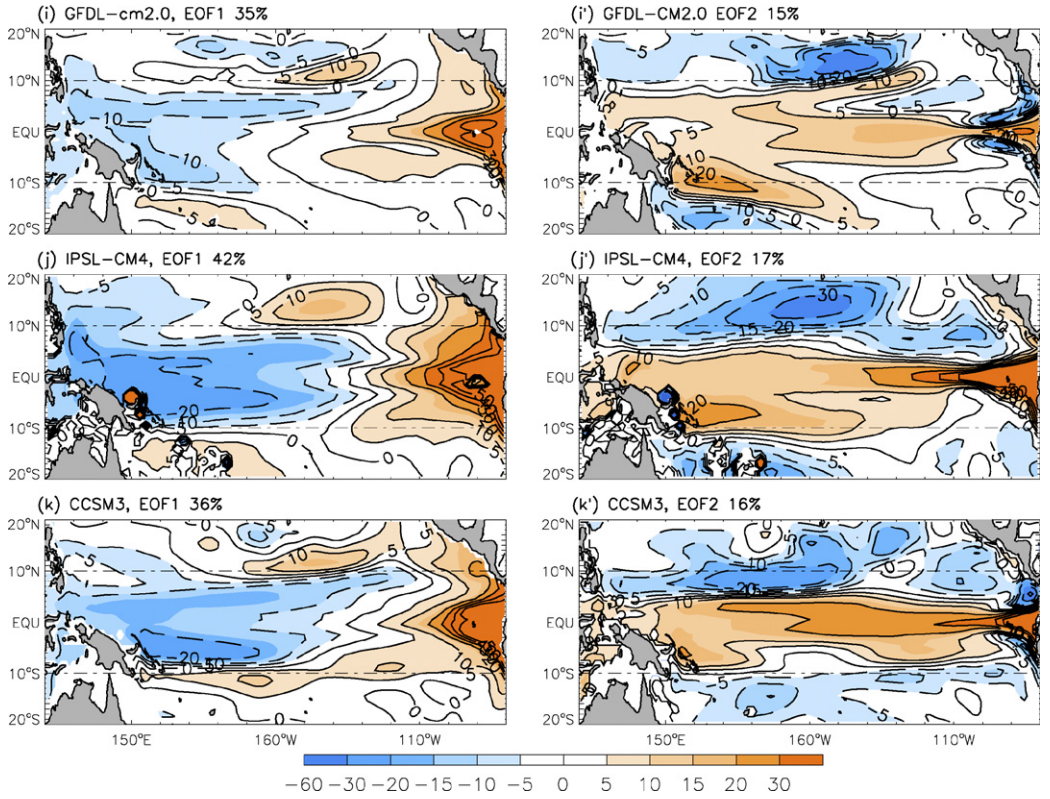

Fig. 5 (*continued*)

thermocline depth anomalies, while the magnitude of τ^x should influence the rate of recharge/discharge (Meinen and McPhaden, 2000). Thus, the zonal wind stress response to interannual SST anomalies in the eastern equatorial Pacific is very important for understanding the characteristics of the modes of thermocline variability.

Fig. 7a–k shows the pattern of zonal wind stress regressed upon the Niño3.4 index for the ocean analysis products and the nine CGCMs. Both the zonal wind stress fields and the Niño3.4 indices have been band-pass filtered prior to the computation of the linear regression using a Fourier filter with half-power at 15 months and 7.5 years, the same filter used for the thermocline depth time series. Regressions are computed at lag 0, since τ^x can be expected to be quasi-simultaneous with the SST anomalies in the eastern equatorial Pacific. Some studies have argued that the zonal location of τ^x can play a significant role in determining the amplitude and timescale of ENSO (An and Wang, 2000; Wittenberg, 2002). Thus, for each model, we have defined a "center of mass" of the regressed wind stress as:

$$C = \frac{\int_0^{L_x} \overline{\tau^x}(x)x\,\mathrm{d}x}{\int_0^{L_x} \overline{\tau^x}\,\mathrm{d}x}, \tag{1}$$

where L_x is the width of the ocean, x is longitude, and $\overline{\tau^x}$ is the anomalous zonal wind stress averaged between 2°S and 2°N at each longitude.

The wind stress patterns for the INGV and GFDL/ARCs analyses, based on the NCEP data (Fig. 7a and b) are centered around 170°W, as indicated by the dot-dash line in Fig. 7a and b, and extend meridionally to approximately 7°N, and 10°–20°S. An estimate of the meridional scale can be obtained from the zero crossings of the zonally averaged τ^x at each latitude. Since we are mainly interested in positive anomalies the zonal average is performed between 154°E and 120°W. The results for the INGV and GFDL/ARCs ocean analyses are shown in Fig. 7a′ and b′. The distance between the points of zero crossings is ~23° for both analyses.

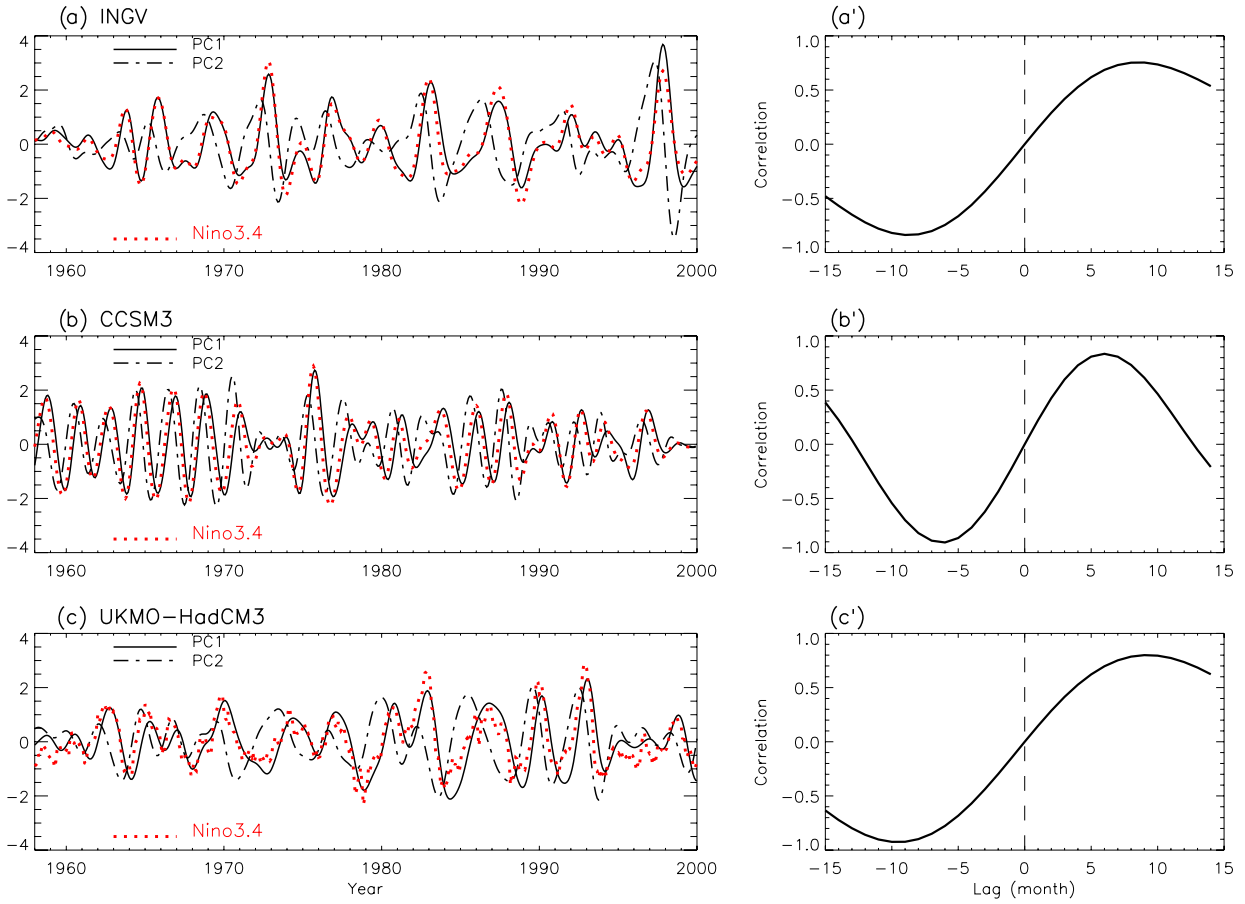

Fig. 6. (a) Leading principal components associated with EOF1 (solid line) and EOF2 (dot-dash line) for the INGV ocean analysis over the period 1958–2000. The Niño3.4 index is also shown for comparison (red dotted line). The correlation coefficient between the Niño3.4 index and PC1 is 0.96, with the Niño3.4 index leading PC1 by 1 month. (a′) Lag-correlation between PC1 and PC2. Negative (positive) lags are for PC1 leading (lagging) PC2. (b) Same as (a), but for CCSM3. The correlation coefficient between Niño3.4 index and PC1 is 0.97, with the Niño3.4 index leading PC1 by 2 months. (b′) Same as (a′), but for CCSM3. (c) Same as (a), but for the UKMO-HadCM3. The correlation coefficient between Niño3.4 index and PC1 is 0.84, with the Niño3.4 index leading PC1 by 3 months. (c′) Same as (a′), but for the UKMO-HadCM3 model.

All the CGCMs are characterized by a meridional scale of τ^x which is narrower than in the observations (Fig. 7c–k). However, there are large differences in the simulated wind stress coupling among the different models. CCSM3, IPSL-CM4, GISS-EH, PCM, CSIRO-Mk3.0, and CNRM-CM3 are characterized by a τ^x structure which is confined within a relatively narrow latitude band around the equator, with nodal lines that are close to zonal. GFDL-CM2.0, UKMO-HadCM3, and to a lesser extent MRI-CGCM2.3.2 have a broader τ^x pattern in the Southern Hemisphere with a southeastward extension which is similar to the one found in observations (Fig. 7a and b). The limited meridional extension of τ^x in the Southern Hemisphere may explain the narrow meridional scale of EOF-2 of thermocline depth for CCSM3, IPSL-CM4, and GISS-EH (Fig. 6c, e, and f), while EOF-2 for PCM, CSIRO-Mk3.0, and CNRM-CM3 has a broader structure in the Southern Hemisphere than the corresponding τ^x. Conversely, the broad southern hemisphere extension of EOF-2 in GFDL-CM2.0, UKMO-HadCM3, and MRI-CGCM2.3.2 seems to be related to that of τ^x.

The τ^x regressions for the different models exhibit a large range of amplitudes, from the large wind stress coupling of the MRI-CGCM2.3.2 model, which has a maximum of 2×10^{-2} Pa °C^{-1} (Fig. 7h) to the relatively weak τ^x response of GISS-EH (Fig. 7e) with a maximum value of $\sim5\times10^{-3}$ Pa °C^{-1}. However, several CGCMs have maximum values of the τ^x regression close to those computed for the INGV and GFDL/ARCs

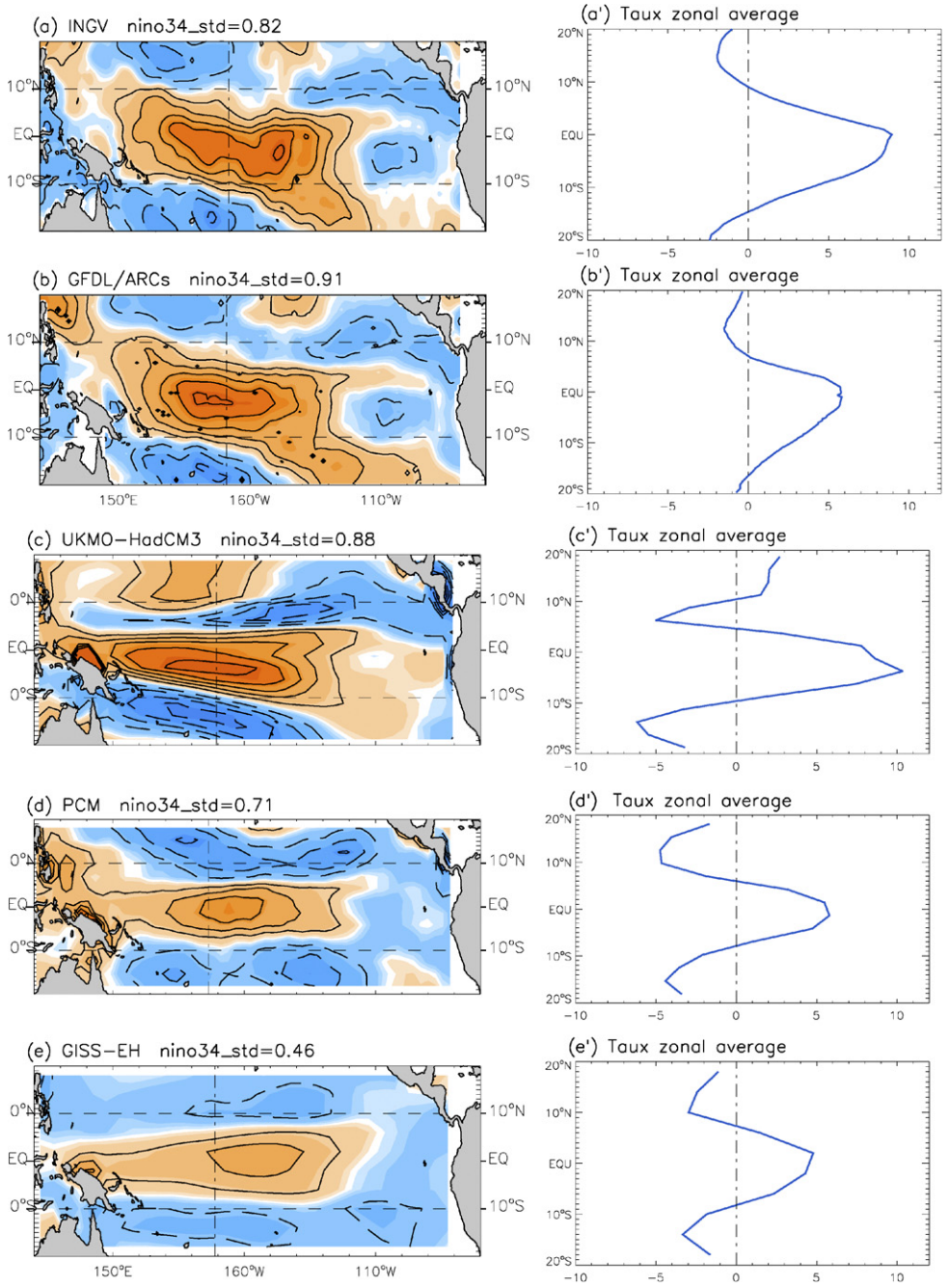

Fig. 7. (a) Regression coefficient of monthly zonal wind stress anomalies upon the Niño3.4 index, based upon monthly values of band-pass filtered data, as described in the text, for the INGV ocean analysis. Contour interval is 2.5×10^{-3} Pa °C^{-1} The dot-dash line indicates the longitude of the "center of mass" of the regressed zonal wind stress within 2°S–2°N, as described in the text. Dashed lines indicate the 10°S, 10°N latitudes, for reference. (a′) Zonal average of (a) between 154°E and 120°W, displayed as a function of latitude. (b) Same as in (a), but for the GFDL/ARCs analysis. (b′) Same as in (a′), but for the GFDL/ARCs analysis. (c) Same as in (a), but for the UKMO-HadCM3. (b′) same as in (a′), but for the UKMO-HadCM3. (d) Same as in (a), but for the PCM. (d′) Same as (a′), but for the PCM. (e) Same as in (a), but for GISS-EH. (e′) Same as (a′), but for the GISS-EH. (f) Same as in (a), but for the CNRM-CM4 model. (f′) Same as in (a′), but for the CNRM-CM4 model. (g) Same as in (a), but for CSIRO-Mk3.0. (g′) Same as in (a′), but for CSIRO-Mk3.0. (h) Same as in (a), but for the MRI-CGCM2.3.2. (h′) Same as in (a′), but for the MRI-CGCM2.3.2. (i) Same as in (a), but for the GFDL-CM2.0 model. (i′) Same as in (a′), but for the GFDL-CM2.0 model. (j) Same as in (a), but for IPSL-CM4. (j′). Same as in (a′), but for IPSL-CM4. (k) Same as in (a), but for CCSM3. (k′) Same as in (a′), but for CCSM3.

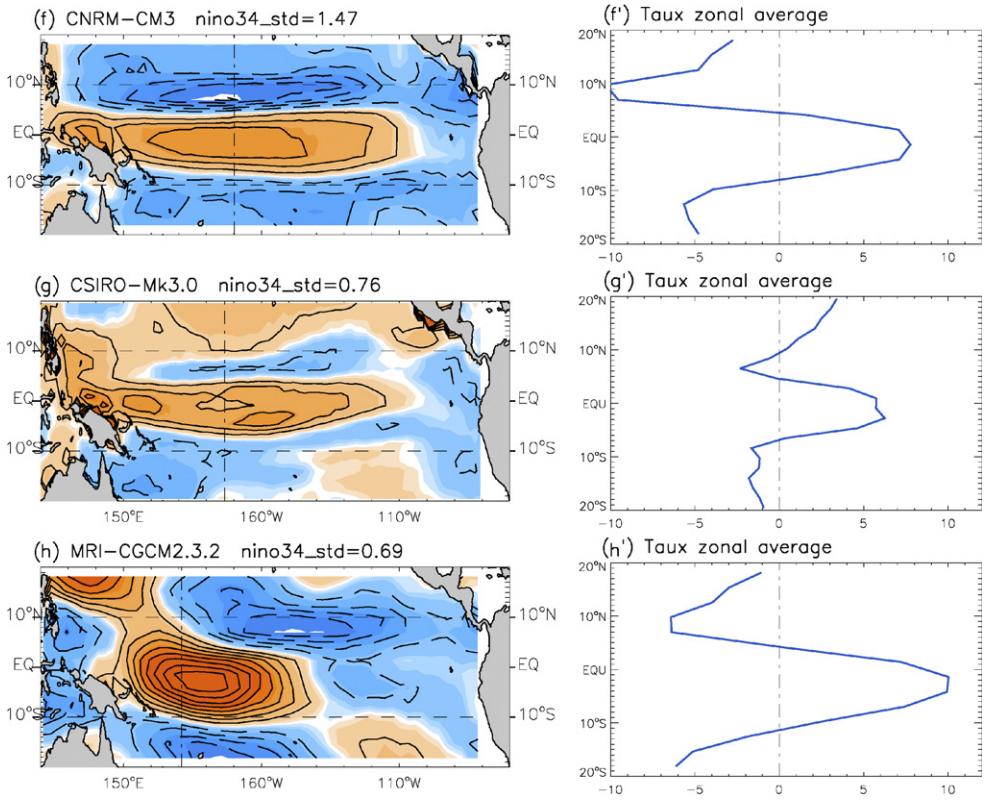

Fig. 7 (*continued*)

ocean analyses, based on the NCEP data (1–1.2 × 10^{-2} Pa °C^{-1}). Another estimate of the wind stress coupling along the equator can be obtained by considering the standard deviation of the interannual τ^x values (band-pass filtered in the 15 mos-7.5 yrs band) averaged over the equatorial region (2°S–2°N and zonally across the basin), and normalized by the standard deviation of the Niño3.4 index. The results, which are shown in Table 2 (τ), indicate that by this measure PCM and GISS-EH have the lowest zonal wind stress sensitivities, with values that are ~36% smaller than in NCEP. For the other CGCMs τ is within 25% of the NCEP value.

4. Which processes determine the ENSO timescale?

ENSO is viewed as the result of a coupled ocean–atmosphere interaction with positive feedbacks promoting the growth of the SST perturbations, and negative feedbacks that limit the amplitude of the anomalies and create the conditions for a phase reversal. Within the "recharge oscillator" paradigm, as described in Section 3, the positive feedback during warm events is provided by the positive zonal wind stress anomalies (the atmospheric response to positive SST perturbations in the eastern equatorial Pacific) which cause a deepening of the eastern equatorial thermocline through the excitation of downwelling Kelvin waves, producing a further amplification of the original SST anomaly (Bjerknes, 1969). The negative feedback is provided by the anomalous poleward transport, a consequence of the altered zonal thermocline tilt, which changes the zonally averaged thermocline depth through the discharge of the warm water volume from the equator. As shown by the EOF analysis in Section 3, the anomalous thermocline tilt (EOF-1) is in phase with the SST perturbations in the eastern equatorial Pacific, while the changes in the zonally average thermocline depth (EOF-2) are approximately in quadrature with the SST variations. Thus, it is the disequilibrium between the zonally averaged thermocline depth and SST (as well as zonal wind stress) anomalies that determines the evolution of the system and allows phase transitions.

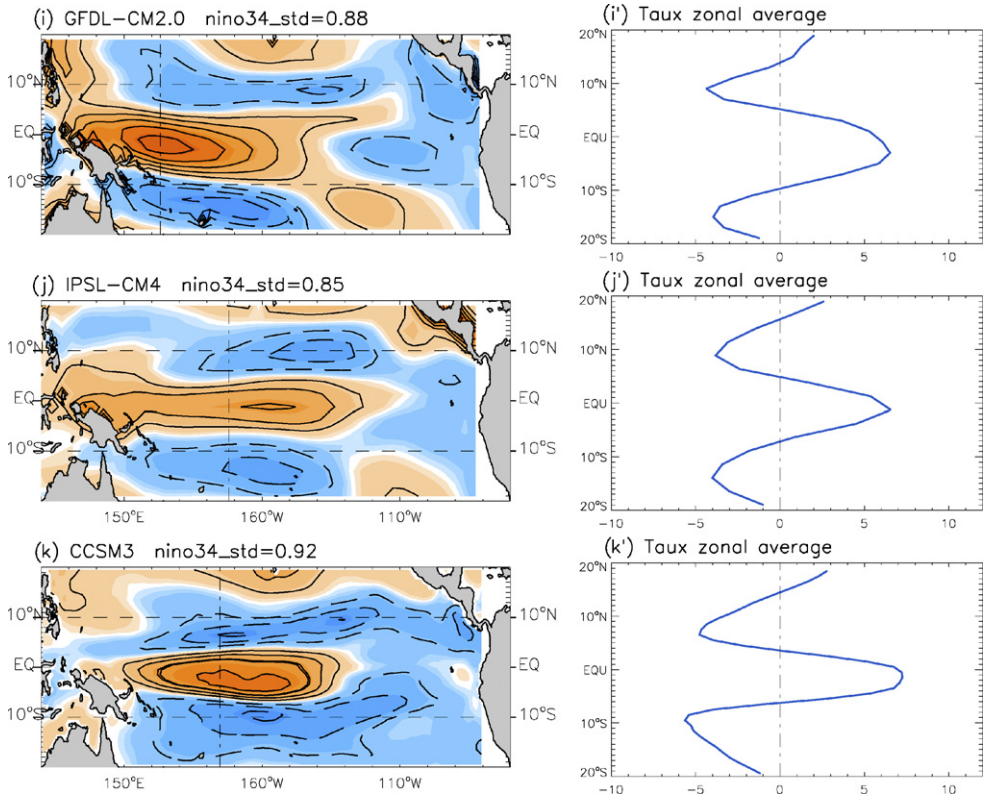

Fig. 7 (*continued*)

The adjustment of the equatorial thermocline involves both equatorially-trapped and extra-equatorial Rossby waves, the former being waves within the 7°S–7°N latitude band, and the latter including Rossby waves forced by the wind stress curl poleward of ±7° (Kirtman, 1997). The westward propagation of the extra-equatorial Rossby waves alters the zonal gradient of thermocline depth, thus allowing the changes in the meridional mass transport responsible for the recharge/discharge of the equatorial thermocline (Capotondi et al., 2005). Wind stress anomalies with a broader meridional structure will excite slower Rossby waves further away from the Equator, and can be expected to lead to a longer adjustment time. The analysis of the zonal wind stress changes associated with the 1976–1977 climate shift (An and Wang, 2000) indicates a broadening of the meridional structure of the anomalous zonal winds, which is consistent with the increase in ENSO period after the mid-seventies. The zonal wind stress anomalies in the CGCMs, as described in Section 3.4, are too tightly confined about the equator compared to observations. Fig. 8a summarizes those results by displaying the dependency of the ENSO timescale upon the meridional scale of the wind stress for the different CGCMs, as well as the INGV analysis. The ENSO timescale for each model has been estimated from the power spectrum of the Niño3.4 index (Fig. 3) as the timescale shorter than 10 years corresponding to the maximum power. The meridional width of the zonal wind stress anomalies (L_y) has been computed from the zonal average of τ^x (Fig. 7a′–k′) as the distance between the latitudes of zero crossings. The values of L_y for the INGV analysis and all the CGCMs are listed in Table 2. Fig. 8(top) shows that there is a large gap between the meridional scale of the wind stress anomalies used to force the INGV analysis (which were derived from NCEP) and those estimated from the CGCMs. While L_y is ∼23° in the INGV analysis, the maximum value of L_y for the CGCMs is less than ∼16°. No clear relationship between period and meridional scale can be detected in Fig. 8(top). This is not surprising, considering that the model climatologies, as well as the strength of the wind stress coupling, differ among CGCMs. For example, Fig. 4 shows that the thermocline structure varies significantly among the different models. Thus, wave phase speeds and transit times can be expected to differ, even if the wind forcing were the same.

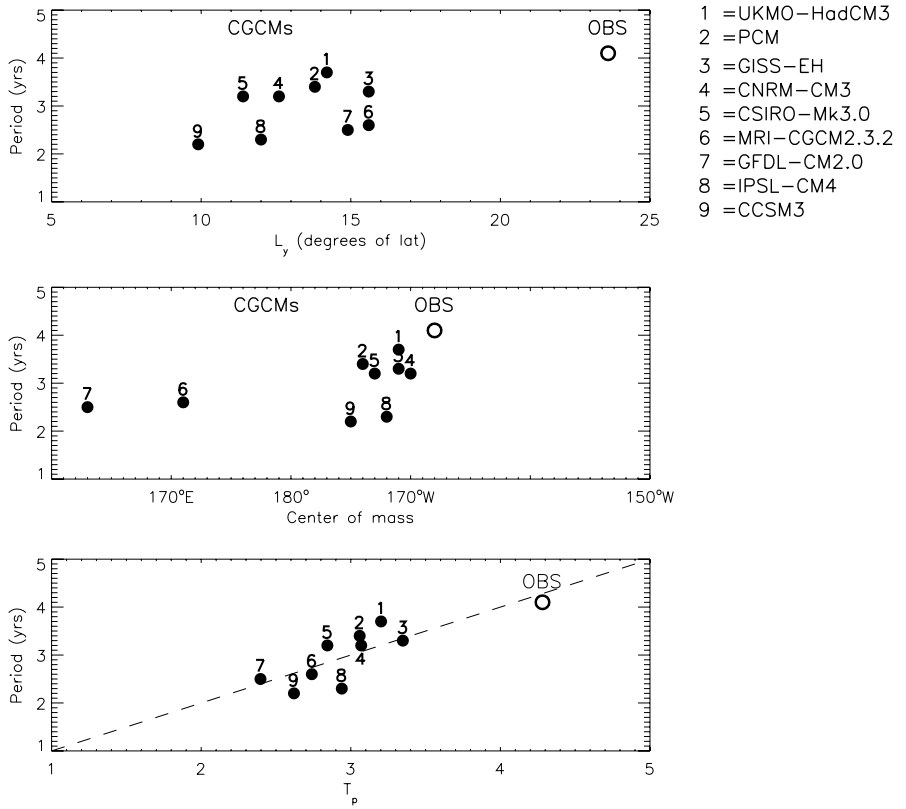

Fig. 8. (Top) ENSO period (defined as the timescales shorter than 10 yrs corresponding to the maximum power in the spectrum of the Niño3.4 index) versus the meridional scale of the wind stress L_y, for all the CGCMs (solid dots) and the INGV ocean analysis (open circle). (Middle) ENSO period versus longitudinal location of the zonal wind stress (computed as the "center of mass" C, defined by Eq. (1) in the text) for all the experiments and the INGV analysis. (Bottom) ENSO period versus T_p, the value of the period predicted by using the multiple regression in Eq. (2).

An and Wang (2000) also noted that the eastward displacement of the wind stress anomalies after the mid-seventies seemed to play an important role in the increase in ENSO period detected after the mid-seventies. Fig. 8(middle) examines the relationship between the period of ENSO and the longitudinal position of τ_x along the equator, as defined by the "center of mass" C (Eq. (1)) for the CGCMs and the INGV analysis. In all the CGCMs the zonal wind stress anomalies are centered more westward than those in the INGV analysis, consistent with the shorter period of ENSO in the CGCMs with respect to observations. However, in some cases the longitude difference is only a few degrees. As for Fig. 8(top), the period of ENSO does not seem to be consistently related solely to the longitudinal position of the wind stress anomalies. The values of C for the INGV analysis and the CGCMs can be found in Table 2.

From Table 2 it is evident that some models have westward-shifted and meridionally wide τ_x' (MRI-CGCM2.3.2), while others have eastward-shifted and meridionally narrow τ_x' (IPSL-CM4). Given these competing effects, it is important to assess the simultaneous dependence of the ENSO period on the parameters in Table 2. To that end we fitted multiple linear regression models of T, using all possible subsets of the three candidate predictors: L_y, C, and τ. Denoting inter-model mean values with an overbar, the best two-predictor linear model was found to have the form

$$T_p = \overline{T} + a(L_y - \overline{L}_y) + b(C - \overline{C}). \tag{2}$$

This model showed a significant ($P < 5.2\%$) reduction in the T residual sum of squares (RSS), below that of the best one-predictor model, which was based on L_y. The best one-predictor model in turn showed a significant ($P < 8.7\%$) reduction in RSS below that of the trivial model $T_p = \overline{T}$. More complex models, which included τ

and/or squared terms, did not further significantly reduce the RSS, and therefore could not be justified based upon the limited sample.

The best-guess parameters for this two-predictor model were estimated via multiple linear regression, and are displayed in the second column of Table 3. To characterize the parameter uncertainty induced by our limited 10-member model sample, we performed two different resampling procedures. Using a jackknife method (Hinkley, 1983), we removed one member and re-fitted the regression model using the remaining nine members. This procedure was repeated nine more times, removing each member in turn, giving a total of 10 new regression models. The maximum and minimum fitted parameters (columns 3 and 4 of Table 3) provide a measure of the robustness of the regression model parameters to the removal of an ensemble member. The second resampling procedure is based on the bootstrap method (Efron and Tibshirani, 1993): a new set of ten members was randomly selected (with replacement) from the individual set of ten (an individual member could appear multiple times, or not at all, in the new set). The regression model was then re-fitted using this new set of ten members. The entire procedure was repeated 10,000 times, and the 5th and 95th percentiles of the re-fitted parameters were estimated to provide a rough measure of the parameter uncertainty (columns 5 and 6 of Table 3). As neither the jackknife not the bootstrapped intervals overlap zero for either a or b, we can infer that at least for this group of GCMs, T does indeed tend to increase with increasing L_y and C.

The characteristics of the wind stress (i.e. L_y and C) influence the evolution of SST anomalies in the eastern equatorial Pacific through heat advection processes. Jin and An (1999), and An et al. (1999) have suggested that among the various advective terms that can alter SST, the mean vertical advection of temperature anomalies ($-\bar{w}T'_z$, where $\bar{w}$ is the temporal mean of the vertical velocity, and T'_z is the vertical gradient of the temperature anomalies, known as the ''thermocline feedback''), and the anomalous zonal advection of the mean zonal temperature gradient ($-u'\overline{T}_x$, where u' is the anomalous zonal velocity, and $\overline{T}_x$ is the zonal gradient of the mean temperature field, the ''zonal advective feedback'') may play a dominant role in ENSO growth and phase transition. Based on an intermediate coupled model, An and Wang (2000) have further shown that the influence of the zonal advective feedback upon ENSO is largely dependent upon the location of the anomalous winds and associated zonal currents. When the zonal wind stress anomalies are displaced eastward (westward), the zonal advective feedback tends to be in phase (quadrature) with the SST anomalies, thus favoring ENSO growth (phase transition), and leading to a longer (shorter) ENSO period. An analysis of the TAO buoy data over the period 1982–1997 (Wang and McPhaden, 2000) has also indicated that anomalous zonal advection of mean temperature gradients, and vertical heat flux at the base of the mixed layer are the dominant terms of the surface layer heat balance in the equatorial Pacific ocean, with the $-u'\overline{T}_x$ term being relatively more pronounced in the central Pacific, and the vertical advection term becoming relatively more dominant in the eastern part of the basin, where the thermocline is shallower.

Are the thermocline and zonal advective feedbacks represented realistically in the CGCMs? Following An and Wang (2000), we compute the lag regressions of $(-\overline{w}T'_z)$ and $(-u'\overline{T}_x)$ upon the Niño3.4 index, as a function of longitude and phase lag, for the two ocean analyses and several CGCMs (Fig. 9). Positive lags indicate that the Niño3.4 index leads the tendency term. The models are sorted as in Table 2, from the longest to the shortest period. The phase lag for each model has been computed by dividing the lag by the period, and multiplying it by 360°. The vertical velocity w is not available for all the CGCMs considered in this study. The lag-regressions are computed only for those models whose output included the w field. All quantities are averaged

Table 3
Fitted values, jackknifed ranges, and bootstrapped 90% confidence intervals for the parameters in Eq. (2)

Parameter	Best guess	Jackknife		Bootstrapped 90%	
		Min	Max	Min	Max
$\overline{T}$	3.05	2.93	3.14	2.74	3.36
$\overline{L_{\bar{y}}}$	14.36	13.33	14.86	12.67	16.35
$\overline{C}$	184.0	183.1	186.3	179.1	188.2
a	0.104	0.084	0.181	0.051	0.26
b	0.0338	0.030	0.043	0.013	0.070
Correl (T, T_{p})	0.82	0.76	0.88	0.67	0.97

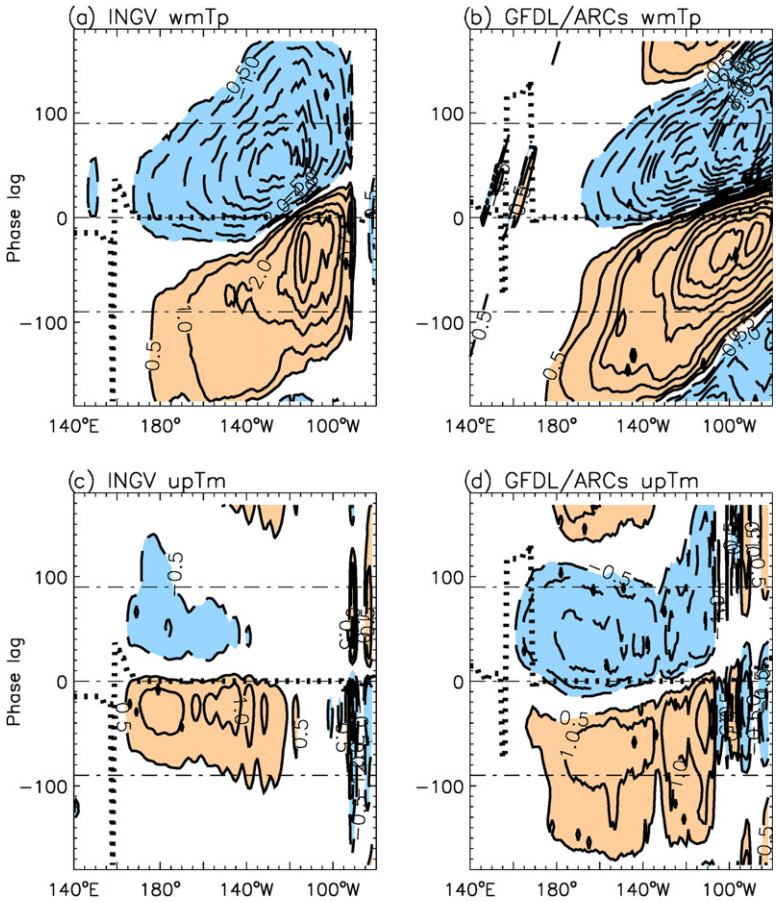

Fig. 9. (a) Regression of the mean vertical advection of temperature anomalies term, $-\bar{w}T'_z$ (wmTp), upon the Niño3.4 index for the INGV ocean analysis. Positive lags indicate that the Niño3.4 index leads the vertical advective tendency. Contour interval is 0.1 °C/month. The ±0.05 contours are also included. Negative values are indicated by dashed contours, while positive values are shown by solid lines. Absolute values larger than 0.05 °C/month are shaded. (c) Regression of the anomalous zonal advection term $-u'\overline{T}_x$ (upTm) upon the Niño3.4 index, displayed as a function of longitude and phase lag for the INGV ocean analysis. Contour interval and shading as in (a). (b) As in (a), but for the GFDL/ARCs analysis. (d) As in (c), but for the GFDL/ARCs analysis. The dot-dash lines in each panel indicate phase lags of −90°, 0°, and +90°. Models are sorted by period (from longest to shortest). The dotted line indicates the lag of maximum correlation between the local SST and the Niño3.4 index. (e) Same as in (a), but for the CNRM-CM3. (h) Same as in (c), but for the CNRM-CM3. (f) Same as in (a), but for CSIRO-Mk3.0. (i) Same as in (c), but for the CSIRO-Mk3.0. (g) Same as in (a), but for MRI-CGCM2.3.2. (j) Same as in (c), but for MRI-CGCM2.3.2. (k) Same as in (a), but for GFDL-CM2.0. (n) Same as in (c), but for GFDL-CM2.0. (l) Same as in (a), but for IPSL-CM4. (o) Same as in (c), but for IPSL-CM4. (m) Same as in (a), but for CCSM3. (p) Same as in (c), but for CCSM3.

between 2°S and 2°N. Temperature and velocity anomalies are computed by subtracting the mean annual cycle from the monthly values of the model outputs. u' is then averaged over the upper 50 m of the water column, roughly corresponding to the depth of the mixed layer, and then multiplied by the zonal gradient of the mean SST to estimate the zonal advective feedback. $\bar{w}$ is computed as the long-term mean vertical velocity in the 2°S–2°N latitude band, at the depth of the maximum upwelling, and the vertical gradient of the temperature anomalies is estimated by considering the difference between T' at the depth of maximum upwelling and the local SST anomalies. In most models the maximum upwelling occurs at ~50–60 m depth (Fig. 10). One exception is the MRI-CGCM2.3.2, whose upwelling maximizes around 20–30 m (Fig. 10e). Since the advective terms affect the local SSTs, to properly evaluate the phase relationship between SST tendencies and SST anomalies at each longitude, the dotted line in each panel of Fig. 9 shows the lag of maximum correlation between the local SST and the Niño3.4 index. In the ocean analyses, SSTs are in phase east of the dateline, where the tendencies achieve the largest regression values with the Niño3.4 index. West of the dateline, the

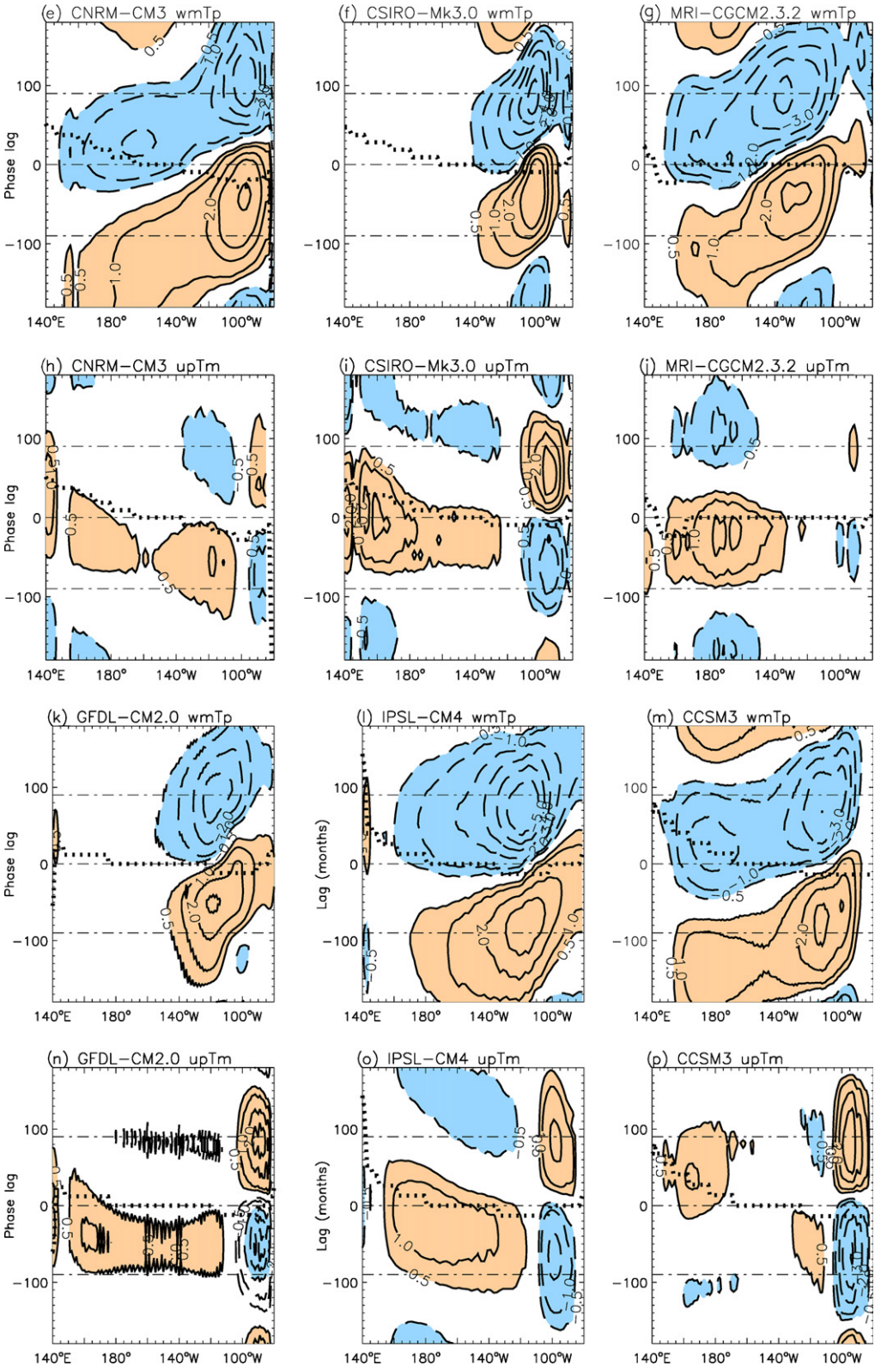

Fig. 9 (*continued*)

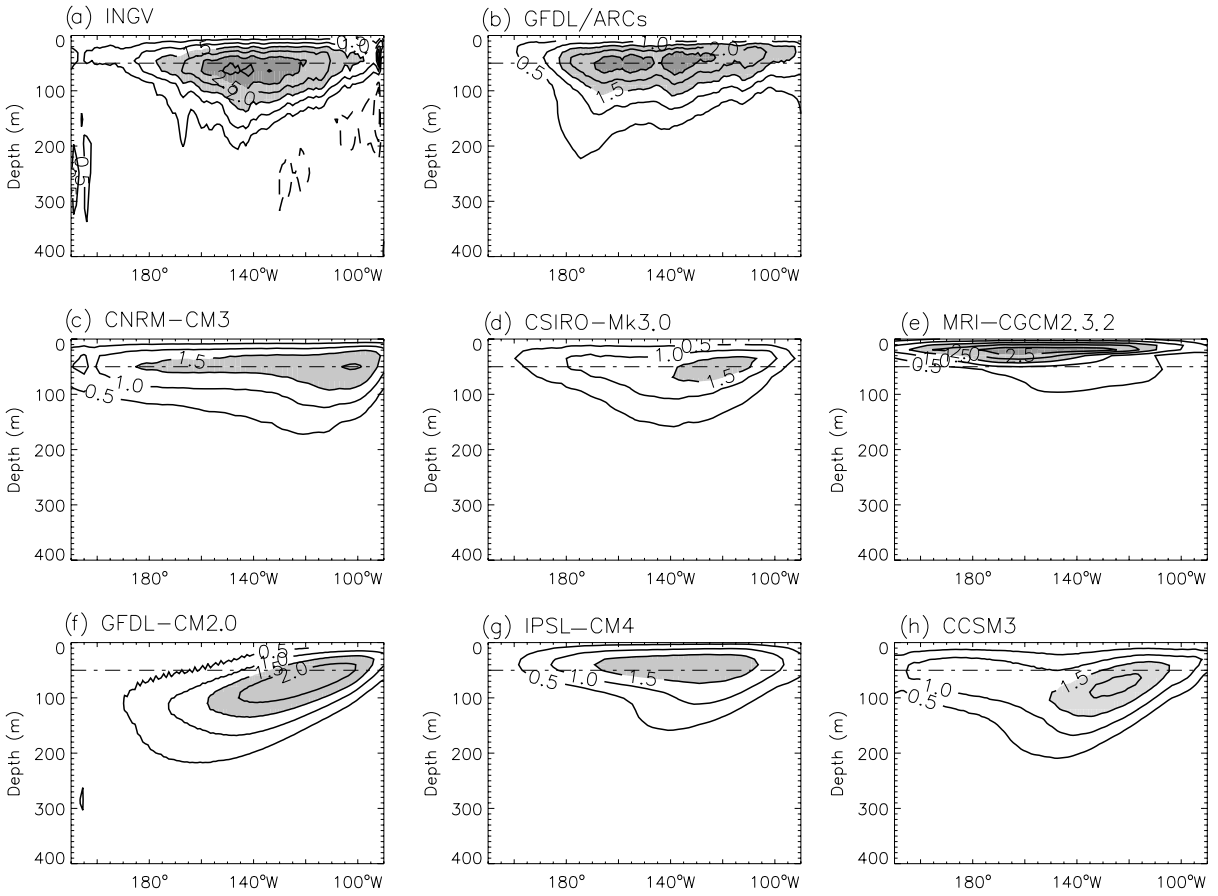

Fig. 10. Time mean vertical velocity, averaged between 2°S and 2°N, and displayed as a function of longitude and depth for the GFDL/ARCs (a), and INGV (b) ocean analyses, and the CGCMs whose output included the vertical velocity field. The dot-dash line indicates 50 m depth, for reference.

phase lags undergo large variations, due to the anticorrelation of SST anomalies in the east and west. Several CGCMs show a slight westward increase of the lags between local SST anomalies and the Niño3.4 index, which is indicative of a westward propagation of the SST anomalies.

In the INGV and GFDL/ARCs analyses the SST tendencies due to the thermocline feedback (Fig. 9a and b) slightly lead the Niño3.4 index east of 140°W. As discussed by An and Wang (2000) and Wittenberg (2002), a tendency term that is in phase with the SST anomaly favors ENSO growth. On the contrary, when the SST tendency is in quadrature with the SST, leading by a quarter cycle, that tendency tends to promote a phase transition. In both ocean analyses, the thermocline feedback leads SST by less than a quarter cycle in the eastern Pacific, thus having both a destabilizing and transitioning influence. Similarly, the positive SST tendencies associated with the zonal advective feedback in the central Pacific also favor both ENSO growth and phase transition in both ocean analyses. In both analysis products, the thermocline feedback is larger than the zonal advective feedback.

In the CGCMs (Fig. 9e–p) the tendencies associated with the thermocline feedback generally lead SST anomalies by less than a quarter cycle, thus promoting ENSO growth as in the ocean analyses. However, in some cases (IPSL-CM4, CCSM3) a large fraction of the thermocline feedback tendency is in quadrature with the SST anomaly, indicating that in these models the thermocline feedback predominantly contributes to ENSO phase transitions. Even in the models where the tendencies associated with the thermocline feedback tend to primarily promote growth, the magnitude of the tendency is generally smaller than in the ocean analyses, a result that may partly arise from the structure of the model mean upwelling. Apart from the MRI-CGCM2.3.2, all the models have a mean upwelling that is weaker than the upwelling in the GFDL/ARCs

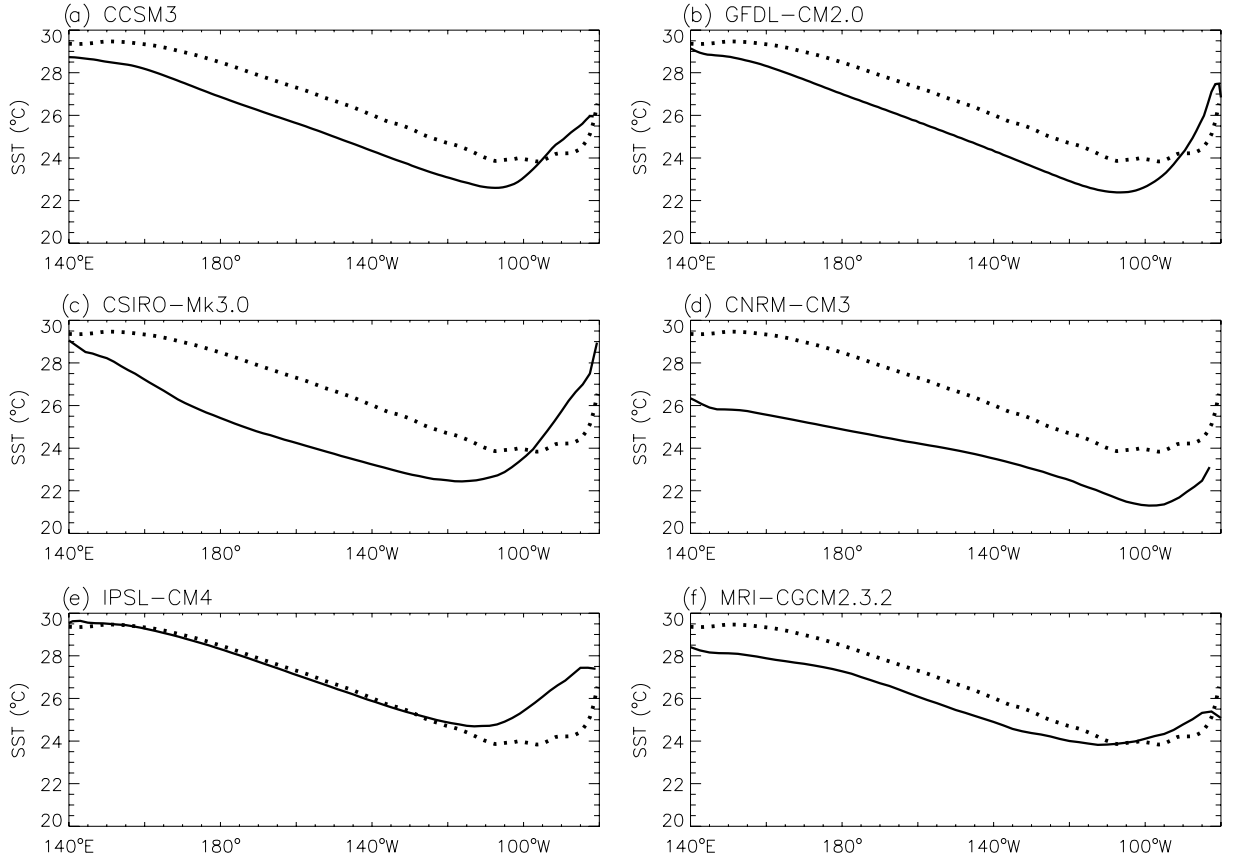

Fig. 11. Solid lines show the longitudinal structure of the mean SST, averaged between 2°S and 2°N for CCSM3 (a), GFDL-CM2.0 (b), CSIRO-Mk3.0 (c), CNRM-CM3 (d), IPSL-CM4 (e), MRI-CGCM2.3.2 (f). The dotted line in each panel shows the longitudinal SST profile for GFDL/ARCs.

and INGV analyses. In the MRI-CGCM2.3.2 the maximum upwelling is comparable in magnitude to that of the ocean analyses, but occurs at a depth which lies within the mixed layer, so that the vertical temperature gradient may not be as large.

The tendencies associated with the zonal advective feedback in the CGCMs generally include a positive component, in the central-western part of the basin, which leads the SST anomalies by less than a quarter cycle, thus promoting ENSO growth as in the ocean analyses. An exception is CCSM3 whose zonal advection tendency is very small west of 110°–120°W. In some models (CSIRO-Mk3.0, GFDL-CM2.0, IPSL-CM4, and CCSM3), the tendencies associated with the zonal advection feedback are negative east of ~110°W. The negative values east of 110°W originate from the positive zonal gradient of mean equatorial SST east of 110°W, which is more pronounced and displaced westward with respect to that in the ocean analyses (Fig. 11). As seen in Fig. 11, the mean zonal structure of SST along the equator has large biases in some of the models. The results in Fig. 9 do not seem to indicate any evident correspondence between the phase relationship of zonal advective feedback and SST anomalies, and the longitudinal position of the zonal wind stress anomalies, as suggested by An and Wang (2000). Further studies are needed to elucidate the processes by which the longitudinal position of τ^x can affect the ENSO timescale in complex coupled models.

The SST tendencies in Fig. 9 seem to indicate the existence of a relationship between the ENSO period and the degree to which the thermocline and advective feedbacks promote ENSO growth, when we consider both their magnitude as well as phase relationship with SST anomalies in the eastern equatorial Pacific. In particular, the relatively large component of the thermocline feedback which is in quadrature with the SST anomalies in IPSL-CM4 and CCSM3 may play an important role in the relative short ENSO period of those models.

5. Conclusions

In this study we have examined the spatial structure and spectral characteristics of the El Niño-Southern Oscillation in nine coupled general circulation models (CGCMs). Observed SSTs, and subsurface data from two ocean analysis products have been used to validate the CGCMs. The interannual SST variations have a realistic amplitude in most models, a factor that represents a significant improvement with respect to earlier versions of the models. However, the patterns of SST variance still show unrealistic aspects. A deficiency which is common to most of the models is the presence of maximum SST variations away from the coast of South America, and in most cases an underestimate of the SST standard deviation along the coast. The westward extension of the SST variance is also generally too large in the models, with cases in which large SST variations are found all the way across the basin.

Interannual SST variations in the climate models are characterized by a dominant timescale which is shorter than observed. An extreme case is CCSM3, whose ENSO-like variability exhibits a quasi-regular two-year cycle.

Changes in the depth of the thermocline are indicative of variations of upper ocean warm water volume that result from the dynamical evolution of the system. The leading modes of variability of thermocline depth in the CGCMs are qualitatively similar to the leading modes of the ocean analysis and to those computed by Meinen and McPhaden (2000) from subsurface observations. The first mode describes variations in the zonal thermocline tilt, and is in phase with SST variations in the eastern equatorial Pacific, while the second mode captures anomalies of the zonally averaged thermocline depth which are approximately in quadrature with the SST anomalies. The two modes describe variations of warm water volume which are consistent with the ''recharge oscillator'' paradigm for ENSO. Differences are found among CGCMs in the exact location of the maximum variability, as well as in the meridional extent of the thermocline depth anomalies. Similarly, there are differences between the patterns of variability from the CGCMs and those derived from observations, the most notable of which is the meridional extent of the thermocline depth anomalies in the southern hemisphere, which is much narrower in the models than in the real world. The meridional scale of the thermocline depth variations is an indication of the volume of warm water involved in the recharge/discharge process, which, within the recharge oscillator paradigm, can be expected to influence the ENSO timescale.

Thermocline variability is primarily controlled by the anomalous surface zonal wind stress. The linear regression of the zonal wind stress upon the Niño3.4 index yields τ^x patterns for the CGCMs characterized by a meridional scale which is narrower than observed, and centered at a longitude which is generally further west than observed. Both factors can affect the ENSO timescale, and may be responsible for some of the discrepancies between the spectral characteristics of ENSO in the models and in the observations.

The pattern of the wind stress can influence the ENSO timescale through two important advective processes: the mean upwelling of temperature anomalies, and the anomalous zonal advection of mean temperature. In the INGV and GFDL/ARCs ocean analyses both processes contribute to ENSO growth, with the thermocline feedback dominating the zonal advective feedback. In the CGCMs the thermocline feedback generally promotes ENSO growth, although the magnitude of the SST tendency is generally smaller than in the ocean analyses, primarily due to the weaker upwelling in the models. In some models (IPSL-CM4, CCSM3) a significant fraction of the tendency associated with the thermocline feedback is in quadrature with the SST anomalies in the eastern equatorial Pacific, indicating that in these models the thermocline feedback can also promote phase transitions. The SST tendencies associated with the zonal advection feedback tend to favor ENSO growth and transition west of ~110°W. In some models tendencies of the opposite sign are found east of 110°W. The longitudinal structure of the mean zonal SST gradient appears to control the sign of the zonal advection tendencies east of 110°W.

Although deficiencies are still present in the coupled simulation of Tropical Pacific interannual variability, the present analysis highlights the improvements that the models have undergone in the past few years in their representation of ENSO. A few years ago, most models still used flux corrections and were severely underestimating or overestimating ENSO variability. The models examined in this study are free of adjustments, and have ENSOs that are much more similar to that observed. A deeper understanding of the exact dynamical

processes responsible for ENSO variability in each model, and of the feedbacks between the oceanic and atmospheric components will be fundamental to further improve the simulation of Tropical Pacific interannual variability in coupled climate models.

Acknowledgments

We acknowledge the international modeling groups for providing their data for analysis, the Program for Climate Model Diagnosis and Intercomparison (PCMDI) for collecting and archiving the model data, the JSC/CLIVAR Working Group on Coupled Modelling (WGCM) and their Coupled Model Intercomparison Project (CMIP) and Climate Simulation Panel for organizing the model data analysis activity, and the IPCC WG1 TSU for technical support. The IPCC Data Archive at Lawrence Livermore National Laboratory is supported by the Office of Science, US Department of Energy. Funding for AC was provided by NOAA. We wish to thank Mike Alexander for his careful reading of the manuscript, and insightful comments. We also thank the two anonymous Reviewers for their constructive criticism and excellent suggestions. The TAO data were provided by the TAO Project Office.

References

AchutaRao, K., Sperber, K.R., 2002. Simulation of the El Niño Southern oscillation: results from the coupled model intercomparison project. Climate Dyn. 19, 191–209.

AchutaRao, K., Sperber, K.R., The CMIP modeling group, 2000. El Niño Southern Oscillation in coupled GCMs. PCMDI Report 61, PCMDI, LLNL, University of California, Livermore, CA, 94550, USA.

Alexander, M.A., Blade, I., Newman, M., Lanzante, J.R., Lau, N.-C., Scott, J.D., 2002. The atmospheric bridge: the influence of ENSO teleconnections on air–sea interaction over the global oceans. J. Climate 15, 2205–2231.

An, S.-I., Wang, B., 2000. Interdecadal change of the structure of the ENSO mode and its impact on the ENSO frequency. J. Climate 13, 2044–2055.

An, S.-I., Jin, F.-F., Kang, I.-S., 1999. The role of zonal advection feedback in phase transition and growth of ENSO in the Cane–Zebiak model. J. Meteorol. Soc. Jpn. 77, 1151–1160.

Atlas, R., Hoffman, R.N., Bloom, S.C., Jusem, J.C., Ardizzone, J., 1996. A multiyear global surface wind velocity dataset using SSM/I wind observations. Bull. Am. Meteorol. Soc. 77, 869–882.

Bjerknes, J., 1969. Atmospheric teleconnections from the equatorial Pacific. Mon. Weather Rev. 97, 163–172.

Cane, M.A., Zebiak, S.E., Dolan, S.C., 1986. Experimental forecasts of El Niño. Nature 321, 827–832.

Capotondi, A., Alexander, M.A., Deser, C., McPhaden, M.J., 2005. Anatomy and decadal evolution of the Pacific Subtropical–Tropical Cells (STCs). J. Climate 18, 3739–3758.

Davey, M.K., Huddleston, M., Sperber, K.R., Model data contributors, 2000. STOIC: a study of coupled GCM climatology and variability in tropical ocean regions. STOIC Project Report, CLIVAR-WGSIP.

Davey, M.K., Huddleston, M., Sperber, K.R., Model data contributors, 2002. STOIC: a study of coupled GCM climatology and variability in tropical ocean regions. Climate Dyn. 18, 403–420.

Derber, J., Rosati, A., 1989. A global oceanic data assimilation system. J. Phys. Oceanogr. 19, 1333–1347.

Deser, C., Phillips, A.S., Hurrel, J.W., 2004. Pacific interdecadal climate variability: linkages between the Tropics and the North Pacific during boreal winter since 1900. J. Climate 17, 3109–3124.

Deser, C., Capotondi, A., Saravanan, R., Phillips, A., 2005. Tropical Pacific and Atlantic climate variability in CCSM3. J. Climate, sub judice.

Efron, B., Tibshirani, R.J., 1993. An Introduction to the Bootstrap. Chapman & Hall, London.

Fedorov, A.V., Philander, S.G., 2000. Is El Niño changing? Science 288, 1997–2002.

Hannachi, A., Stephenson, D.B., Sperber, K.R., 2003. Probability-based methods for quantifying nonlinearity in the ENSO. Climate Dyn. 20, 241–256.

Hinkley, D., 1983. Jackknife methods. In: Kotz, S., Johnson, N.L., Read, C.B. (Eds.), Encyclopedia of Statistics, vol. 4. Wiley, New York.

Hoerling, M., Kumar, A., 2003. The perfect ocean for drought. Science 299, 691–694.

Jin, F.-F., 1997a. An equatorial ocean recharge paradigm for ENSO. Part I: conceptual model. J. Atmos. Sci. 54, 811–829.

Jin, F.-F., 1997b. An equatorial ocean recharge paradigm for ENSO. Part II: a stripped-down coupled model. J. Atmos. Sci. 54, 830–847.

Jin, F.-F., An, S.-I., 1999. Thermocline and zonal advective feedbacks within the equatorial ocean recharge oscillator model for ENSO. Geophys. Res. Lett. 26, 2989–2992.

Kalnay, E. et al., 1996. The NCEP/NCAR 40-year reanalysis project. Bull. Am. Meteorol. Soc. 77, 437–472.

Kirtman, B.P., 1997. Oceanic Rossby wave dynamics and the ENSO period in a coupled model. J. Climate 10, 1690–1704.

Kistler, R. et al., 2001. The NCEP–NCAR 50-year reanalyses: monthly means CD-ROM and documentation. Bull. Am. Meteorol. Soc. 82, 247–267.

Latif, M. et al., 2001. ENSIP: the El Niño simulation intercomparison project. Climate Dyn. 18, 255–276.

Masina, S., Di Pietro, P., Navarra, A., 2004. Interannual-to-decadal variability of the North Atlantic from an ocean data assimilation system. Climate Dyn. 23, 531–546.

McPhaden, M.J. et al., 1998. The Tropical ocean global atmosphere (TOGA) observing system: a decade of progress. J. Geophys. Res. 103 (14), 169–240.

Meinen, C.S., McPhaden, M.J., 2000. Observations of warm water volume changes in the equatorial Pacific and their relationship to El Niño and La Niña. J. Climate 13, 3551–3559.

Schneider, E.K., Huang, B., Shukla, J., 1995. Ocean wave dynamics and El Niño. J. Climate 8, 2415–2439.

Trenberth, K.E., 1997. The definition of El Niño. Bull. Am. Meteorol. Soc. 78, 2771–2777.

Wang, W., McPhaden, M.J., 2000. The surface-layer heat balance in the equatorial Pacific Ocean. Part II: interannual variability. J. Phys. Oceanogr. 30, 2989–3008.

Wittenberg, A.T., 2002. ENSO response to altered climates. Ph.D. thesis, Princeton University, 475 pp.

Wittenberg, A.T., Rosati, A., Lau, N.-C., Ploshay, J.J., 2006. GFDL's CM2 global coupled climate models. Part 3: Tropical Pacific climate and ENSO. J. Climate. 19, 698–722.

Wyrtki, K., 1985. Water displacements in the Pacific and the genesis of El Niño cycles. J. Geophys. Res. 90, 7129–7132.